
Constrained Diffusion Models with Primal-Dual Inference

Samar Hadou Yiğit Berkay Uslu Alejandro Ribeiro
Department of Electrical and Systems Engineering
University of Pennsylvania
{selaraby,ybuslu,aribeiro}@seas.upenn.edu

Abstract

This paper develops constrained diffusion models with primal-dual inference (PDI) to sample from optimal distributions of entropy-regularized optimization problems with *average* constraints. We formalize constrained sampling in the Lagrangian dual domain, where the optimal distribution takes the form of a Gibbs distribution indexed by the optimal dual variable. Rather than estimating this dual multiplier before sampling and freezing it throughout generation, PDI jointly infers the optimal primal distribution and its parametrizing dual variable. Each reverse diffusion step denoises using the score field associated with the current multiplier and then updates the multiplier through dual ascent using the estimated constraint violation of the denoised samples. To enable this conditional score field, we train a single dual-conditioned score network over the family of Gibbs distributions induced by the dual variables encountered during inference. We prove that the time average of the dual variables generated along the inference trajectory converges to a neighborhood of the dual optimum and bound the effect of residual dual mismatch on the terminal distribution through schedule-dependent stability factors. We evaluate PDI on constrained sampling from a mixture of Gaussians, wireless resource allocation, and portfolio management.

1 Introduction

Diffusion models have become a dominant framework for sampling from complex, high-dimensional distributions by learning to reverse a noising process [1, 2, 3]. While their most apparent successes lie in unconstrained perceptual tasks such as image [4], audio [5], and video synthesis [6], the same distributional modeling capabilities are valuable for tackling a broad class of constrained optimization problems, whose optimal solutions are probabilistic rather than deterministic. Wireless resource allocation, for instance, employs stochastic, time-sharing policies to maximize a network-wide utility, subject to per-user service guarantees [7, 8]. Similarly, portfolio management seeks to diversify allocations to maximize returns under expected risk constraints [9, 10]. Standard diffusion models, however, lack reliable mechanisms to enforce such statistical constraints during sampling. This paper develops diffusion models with primal-dual inference to bridge that gap.

Entropy-regularized formulations that optimize over distributions with average constraints admit a clean form in the Lagrangian dual domain. For a fixed dual variable, the distributional minimizer of the Lagrangian is a Gibbs distribution whose energy is linear in the dual variable. This connects constrained sampling to the vast literature on diffusion-based samplers from unnormalized Gibbs targets [11, 12, 13, 14]. In principle, one could solve for the optimal dual variable, and train a diffusion model to sample from the corresponding Gibbs distribution. In our setting, however, the sampler must operate over a family of constrained optimization instances and each instance can induce a different optimal multiplier. Estimating these multipliers before sampling is fragile and expensive. The optimal multiplier is defined through intractable expectations under the Gibbs distribution, so each dual

update requires estimating statistics of the very distribution being learned. Prior dual-training (DT) approaches [15, 16] address this by alternating dual updates with score-model training. With only a limited number of score updates per dual iterate, the learned score model can reflect the accumulated history of these targets rather than the Gibbs score field indexed by the final multiplier. Once training ends, the resulting sampler is fixed and cannot respond to constraint violations during generation.

This paper proposes a different view. Rather than treating the dual variable as a quantity that must be estimated before sampling, we make it part of the sampling state. We propose primal–dual inference (PDI), which interleaves dual ascent with the reverse diffusion process. At each denoising step, PDI uses the score field associated with the current multiplier to update the samples, estimates constraint violations from Tweedie-based estimates of denoised samples [17], and updates the multiplier before the next reverse step. The dual variable becomes an inference-time state of the sampler that steers the trajectories toward feasibility, and the sampler follows a path-dependent sequence of Gibbs score fields. This dynamic coupling keeps the score field aligned with the current multiplier throughout inference and allows early noisy steps to absorb dual mismatch while later steps refine samples under multipliers that have already reached a region close to the optimal multiplier. Our analysis captures this effect by proving convergence of the time-averaged dual variables and bounding how residual dual mismatch propagates through the reverse process.

To enable this primal–dual coupling, we train a single score network conditioned on the dual variable, so that the model represents a family of Gibbs targets rather than a single constrained distribution. This gives PDI a direct mechanism for adapting to shifted constraints and out-of-distribution (OOD) instances, as long as the induced dual trajectory remains within the multiplier range covered during training. Empirically, we show that PDI outperforms DT and remains more robust under shifted constraints. When DT is strengthened by freezing a candidate final multiplier and continuing score training for that fixed Gibbs target, it becomes competitive with PDI, but only after this additional training stage. This shows that PDI’s advantage is not merely estimating a good multiplier, but keeping multiplier updates coupled to the denoising trajectory during inference.

We make the following contributions.

- (C1) We cast constrained sampling with average constraints as a saddle-point problem in the Lagrangian dual domain, where the optimal distribution is a Gibbs distribution indexed by the optimal dual variable.
- (C2) We introduce the PDI algorithm, a reverse-diffusion sampler in which primal denoising and dual ascent evolve jointly. At each step, the sampler uses the score field associated with the current multiplier and then updates the multiplier using constraint violations.
- (C3) We train a single dual-variable-conditioned score network that generalizes across the family of Gibbs distributions indexed by the dual variable encountered during inference.
- (C4) We establish convergence of the time-averaged dual iterates to a neighborhood of the optimal multiplier. We also bound the effect of residual dual mismatch on the terminal distribution through schedule-dependent stability factors.
- (C5) We validate PDI empirically on a constrained Gaussian mixture, a wireless power-control problem with per-user rate requirements, and a portfolio-construction task with expected risk constraints.

Figure 1 makes the effect of inference-time dual updates concrete. We showcase a wireless optimization problem where users share a channel and each needs a minimum average service rate. An unconstrained sampler ignores the requirements and leaves many users underserved; DT denoises dual variables before sampling and so cannot correct violations during generation; and PDI, by updating the dual variables as it denoises, steers samples toward (average) feasibility and lifts the worst-served users much closer to their targets.

2 Related Work

Diffusion model sampling with constraints. Guidance techniques steer reverse diffusions toward reward or constraint alignment by modifying the score in Tweedie’s denoising formula [17], as in classifier guidance [18], classifier-free guidance [19], and CLIP-based variants [20]. A separate line of work enforces domain-feasibility constraints directly on the diffusion process through boundary reflections [21], mirror maps [22], Riemannian formulations [23], log-barrier constructions [24],

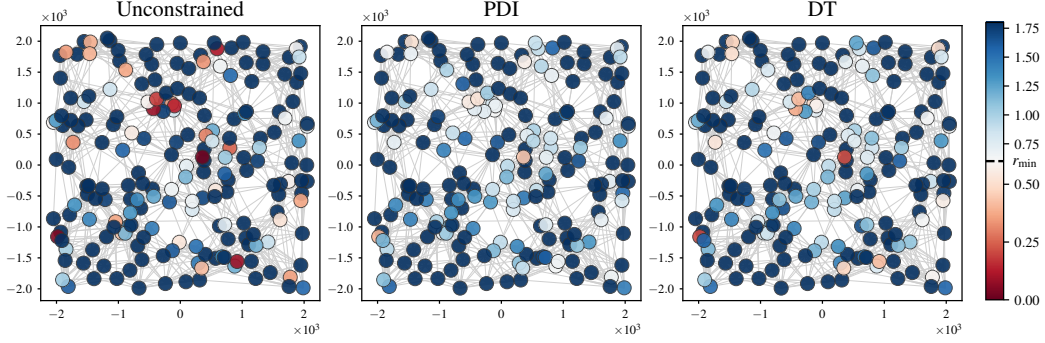


Figure 1: **Wireless power allocation under ergodic minimum-rate r_{\min} constraints.** Nodes represent users and colors indicate how well the rate requirement of each user is met, with red marking those that fall short. Here, average constraints are meaningful because mutual interference prevents any single solution from satisfying every requirement at once. Optimal solutions must therefore alternate samples (i.e., power allocations and/or channel access) over time, so that some compensate for others. The unconstrained sampler leaves many users below the target rate (red nodes), while DT partially improves feasibility through training-time dual updates. PDI further improves the lower-rate users by updating the dual variables during denoising.

feasibility projections [25], and constrained reverse steps [26]. Most importantly, these methods address pointwise constraints rather than distributional (average) ones.

Constrained diffusion modeling with Lagrangian dual formulations. Closely related to our work are [15, 16, 27], which adopt primal–dual formulations for average constraints. Specifically, [15, 16] pair outer-loop dual ascent with inner-loop score matching but retrain the score network for each dual iterate, while primal–dual Langevin Monte Carlo [27] jointly evolves samples and multipliers at sampling time but forgoes a learned generative model. Our method shares the Lagrangian saddle-point structure of these works but differs in two key aspects. First, the dual variables evolve jointly with the denoising trajectory rather than in a separate training loop or ergodic Langevin chain. Second, a single score network, conditioned on the dual variable, is trained across a distribution of multipliers rather than refitted per iterate. An extended related work is provided in Appendix A.

3 Constrained Diffusion Models

Consider a target distribution μ^* that trades off minimization of a variational objective function with satisfying a set of constraints in expectation. More concretely, μ^* is the minimizer of

$$\begin{aligned}
 P^* &= \min_{\mu \in \mathcal{P}_2} \mathbb{E}_{\mu} [f_0(\mathbf{x})] - \beta \mathcal{H}(\mu), \\
 \text{s.t. } &\mathbb{E}_{\mu} [\mathbf{f}(\mathbf{x})] \preceq \mathbf{0},
 \end{aligned} \tag{1}$$

where $f_0 : \mathcal{X} \rightarrow \mathbb{R}$, $\mathbf{f} : \mathcal{X} \rightarrow \mathbb{R}^d$, $\mathcal{X} \subseteq \mathbb{R}^p$ is the domain of feasible decisions and $\mathcal{P}_2(\mathcal{X})$ denotes the space of all probability distributions supported on \mathcal{X} with finite second moments. We augment the objective with an entropy regularization term to penalize degenerate solutions and ensure sample diversity. This formulation is particularly relevant in multi-player cooperative games and resource allocation problems, where a single deterministic policy may not satisfy all competing requirements simultaneously. In such settings, time-sharing policies sampled from μ^* can satisfy the constraints on average while improving the tradeoff between optimality and feasibility.

The problem in (1) is (β -strongly) convex in μ with zero duality gap and can be handled in the dual domain by constructing the Lagrangian function,

$$\mathcal{L}(\mu, \boldsymbol{\lambda}) = \mathbb{E}_{\mathbf{x} \sim \mu} [f_0(\mathbf{x}) + \boldsymbol{\lambda}^\top \mathbf{f}(\mathbf{x})] - \beta \mathcal{H}(\mu), \tag{2}$$

where $\boldsymbol{\lambda} \succeq \mathbf{0}$ contains the Lagrangian multipliers. The dual problem is then defined as

$$D^* = \max_{\boldsymbol{\lambda} \succeq \mathbf{0}} \min_{\mu \in \mathcal{P}_2} \mathbb{E}_{\mathbf{x} \sim \mu} [f_0(\mathbf{x}) + \boldsymbol{\lambda}^\top \mathbf{f}(\mathbf{x})] - \beta \mathcal{H}(\mu). \tag{3}$$

The two problems are equivalent by the following proposition.

Assumption 1 (Existence of a strictly feasible solution). *There exists $\mu' \in \mathcal{P}_2$ such that $\mathbb{E}_{\mu'} [f_0(\mathbf{x})] - \beta \mathcal{H}(\mu') < C < \infty$, and $\mathbb{E}_{\mu'} [\mathbf{f}(\mathbf{x})] \preceq -\xi \mathbf{1} \prec \mathbf{0}$.*

Proposition 1 (Strong duality [27]). *Under Assumption 1, and for $\beta > 0$, we have $P^* = D^*$, and the optimal pair (μ^*, λ^*) is a saddle-point of the Lagrangian, i.e., $\mathcal{L}(\mu^*, \lambda) \leq \mathcal{L}(\mu^*, \lambda^*) \leq \mathcal{L}(\mu, \lambda^*)$, for any $\mu \in \mathcal{P}_2(\mathcal{X})$ and $\lambda \in \mathbb{R}_+^d$. It also holds that λ^* is finite, i.e., $\lambda^* \in \Lambda \subset \mathbb{R}_+^d$. Moreover, μ^* follows the law of the Gibbs distribution,*

$$\mu^*(\mathbf{x}) = \mu_{\lambda^*}(\mathbf{x}) = \frac{1}{Z(\lambda^*)} \cdot \exp\left(-\frac{1}{\beta}(f_0(\mathbf{x}) + \lambda^{*\top} \mathbf{f}(\mathbf{x}))\right), \quad (4)$$

with $Z(\lambda^*) = \int \exp\left(-\frac{1}{\beta}(f_0(\mathbf{x}) + \lambda^{*\top} \mathbf{f}(\mathbf{x}))\right) d\mathbf{x}$.

Proposition 1 shows that the optimal distribution is a Gibbs distribution parametrized by the optimal dual variable, which can equivalently be viewed as an exponential tilting of the implicit uniform prior on \mathcal{X} . Since the energy functions are known, sampling from this distribution is straightforward in principle. However, a computational challenge lies in that the optimal dual multiplier satisfies a saddle-point condition involving expectations under the very distribution it parametrizes. Prior work [15] addresses this by estimating λ^* through a dual-training loop wrapped around diffusion-based score matching. However, this requires retraining or fine-tuning the score network for each dual iterate, let alone each new problem instance, and leaves a fixed sampler after training. To alleviate these challenges, we propose the PDI algorithm, which shifts the search for λ^* from training to inference.

3.1 Primal–Dual Inference

For a given λ , the inner minimizer of the Lagrangian in (3) is the Gibbs distribution

$$\mu_{\lambda}^{\dagger}(\mathbf{x}) \propto \exp\left(-E(\mathbf{x}, \lambda)\right), \quad E(\mathbf{x}, \lambda) = \frac{1}{\beta}\left(f_0(\mathbf{x}) + \lambda^{\top} \mathbf{f}(\mathbf{x})\right), \quad (5)$$

where the energy function E is the point-wise Lagrangian function scaled by β . We utilize diffusion models to sample from the family of Gibbs distributions $\{\mu_{\lambda}^{\dagger} \mid \lambda \in \Lambda\}$. If $\lambda = \lambda^*$, this Gibbs distribution coincides with the optimal constrained distribution μ^* .

Diffusion models learn the reverse dynamics of a Gaussian noising process initialized at the target distribution [3]. For each Gibbs distribution, we define a forward process,

$$\mathbf{y}_{\tau}(\lambda) = \sqrt{a_{\tau}} \mathbf{y}_{\tau-1}(\lambda) + \sqrt{b_{\tau}} \epsilon_{\tau}, \quad \mathbf{y}_0(\lambda) \sim \mu_{\lambda}^{\dagger}, \quad \mathbf{y}_T \sim \mathcal{N}(\mathbf{0}, \mathbf{I}), \quad (6)$$

with $\epsilon_{\tau} \sim \mathcal{N}(\mathbf{0}, \mathbf{I})$. All processes in this family share the same decay schedule $\{a_{\tau}\}$, noise schedule $\{b_{\tau}\}$ and terminal distribution $\mathcal{N}(\mathbf{0}, \mathbf{I})$. We reserve the subscript τ for the time of the forward processes running from 0 to T . Each forward process induces a forward marginal distribution $q_{\tau}^{\lambda} := q_{\tau}(\cdot \mid \lambda)$. The conditional distribution at time τ is $q_{\tau \mid 0}(\cdot \mid \mathbf{y}_0, \lambda) = \mathcal{N}(\alpha_{\tau} \mathbf{y}_0, \sigma_{\tau}^2 \mathbf{I})$ with $\alpha_{\tau} = \prod_{s=1}^{\tau} \sqrt{a_s}$, and $\sigma_{\tau}^2 = \sum_{j=1}^{\tau} b_j \prod_{s=j+1}^{\tau} a_s$. Throughout the paper, we refer to $\text{SNR}_{\tau} := \alpha_{\tau}^2 / \sigma_{\tau}^2$ as the signal-to-noise ratio. For a fixed λ , we associate to the forward process a score-based reverse sampler,

$$\mathbf{x}_{t+1}(\lambda) = \frac{1}{\sqrt{a_{T-t}}} \left(\mathbf{x}_t(\lambda) + b_{T-t} \nabla \log q_{T-t}(\mathbf{x}_t \mid \lambda) \right) + \sqrt{b_{T-t}} \epsilon_t, \quad (7)$$

with $\mathbf{x}_0 \sim \mathcal{N}(\mathbf{0}, \mathbf{I})$, $\mathbf{x}_T(\lambda) \sim \mu_{\lambda}^{\dagger}$, and $\epsilon_t \sim \mathcal{N}(\mathbf{0}, \mathbf{I})$. We use the subscript t to refer to the inference time running from Gaussian noise to the target distribution with $t = T - \tau$. The reverse process induces marginal distributions $\tilde{p}_t(\cdot \mid \lambda)$ that ideally match those of the forward process, namely $\tilde{p}_t \approx q_{T-t}$, for all λ .

Running (7) under the optimal value λ^* produces samples from the optimal distribution $\mu_{\lambda^*}^{\dagger}$, which coincides with μ^* under strong duality. PDI replaces this fixed-multiplier sampler with a time-varying reverse process whose multiplier is updated during inference through dual ascent. Each reverse step uses the Gibbs score field indexed by the current multiplier, and the multiplier is updated from the constraint residual evaluated on Tweedie posterior-mean estimates:

$$\mathbf{x}_{t+1} = \frac{1}{\sqrt{a_{T-t}}} \left(\mathbf{x}_t + b_{T-t} \nabla_{\mathbf{x}_t} \log q_{T-t}(\mathbf{x}_t \mid \lambda_t) \right) + \sqrt{b_{T-t}} \epsilon_t, \quad (\text{PDI-P})$$

$$\lambda_{t+1} = \left[\lambda_t + \eta_t \mathbb{E}_{\mathbf{x}_{t+1}} \left[\mathbf{f} \left(\mathbb{E}[\mathbf{y}_0 \mid \mathbf{x}_{t+1}, \lambda_t] \right) \right] \right]_+. \quad (\text{PDI-D})$$

The operator $[\cdot]_+$ denotes the projection onto the nonnegative orthant, η_t is the dual step size, and $\mathbb{E}[\mathbf{y}_0 | \mathbf{x}_{t+1}, \boldsymbol{\lambda}_t]$ is the Tweedie posterior-mean estimate of the clean samples under the forward process initialized at $\mu_{\boldsymbol{\lambda}_t}^\dagger$. The primal step uses the score of the forward marginal q_{T-t} selected by the current multiplier, while the dual step updates the multipliers in the direction of the average constraint violation estimated from the Tweedie clean-sample estimates. The primal samples and dual variable therefore evolve together during generation. As the dual iterates approach a neighborhood of $\boldsymbol{\lambda}^*$, the sampler is steered through Gibbs distributions indexed by near-optimal multipliers.

Remark 1. *The dual update in (PDI-D) evaluates the constraint violations over an ensemble of samples, reflecting the fact that the constraints are imposed in expectation and must therefore be assessed on average. This is in contrast with other constrained diffusion and sampling methods, e.g., [25, 27, 28], which enforce constraints separately on each sample. In our implementation of PDI, we run multiple sampling chains in parallel, each of which tracks a separate multiplier, as described in Algorithm 2. This scheme preserves the average-constraint interpretation while providing robustness to perturbations in the final dual estimate.*

3.2 Score Network Training

PDI requires access to the score field $\nabla_{\mathbf{x}_t} \log q_{T-t}(\mathbf{x}_t | \boldsymbol{\lambda}_t)$ for the multiplier encountered at each denoising step. Since this score is not available in closed form, we learn a dual-conditioned score model $s_\theta(\mathbf{x}_t, t, \boldsymbol{\lambda}_t)$ that approximates the family of noised Gibbs score fields indexed by $\boldsymbol{\lambda}$. The primal update in (PDI-P) is then replaced with

$$\mathbf{x}_{t+1} = \frac{1}{\sqrt{a_{T-t}}} \left(\mathbf{x}_t + b_{T-t} s_\theta(\mathbf{x}_t, t, \boldsymbol{\lambda}_t) \right) + \sqrt{b_{T-t}} \boldsymbol{\epsilon}_t. \quad (8)$$

The score model is trained across a family of problem instances parameterized by \mathcal{G} . Thus, the score model formally depends on the problem instance and should be written as $s_\theta(\mathbf{x}_t, t, \boldsymbol{\lambda}_t, \mathcal{G})$. To keep the notation uncluttered, we suppress the explicit dependence on \mathcal{G} and write $s_\theta(\mathbf{x}_t, t, \boldsymbol{\lambda}_t)$ throughout.

The score model is trained to approximate the score of the Gibbs distribution indexed by different dual variables. The training objective is

$$\boldsymbol{\theta}^* \in \operatorname{argmin}_{\boldsymbol{\theta}} \mathbb{E}_{\boldsymbol{\lambda}, \mathbf{x}_t, t} \left[\omega(t) \| s_\theta(\mathbf{x}_t, t, \boldsymbol{\lambda}) - \nabla_{\mathbf{x}_t} \log q_{T-t}(\mathbf{x}_t | \boldsymbol{\lambda}) \|_2^2 \right], \quad (9)$$

where $\omega(t)$ is a time-dependent weighting function. The expectation is taken over diffusion times, noisy samples, a training distribution of problem instances and dual variables. This differs from standard denoising or score-matching objectives in two ways. First, the relevant distribution over dual variables is not known in advance because it is induced by the inference-time dual trajectory. Second, unlike computer vision tasks, where training starts from samples of the target distribution, our starting point is the optimization problem in (1), whose solution distributions and samples are not necessarily available a priori.

To mitigate these two issues, we propose Algorithm 1 in Appendix B. The training procedure starts by sampling dual multipliers from a prior distribution and rolling out trajectories using the untrained score network to collect noisy samples \mathbf{x}_t . As training progresses, we sample pairs $(\mathbf{x}_t, \boldsymbol{\lambda}_t)$ along these trajectories instead of relying on the initial prior alone. For each pair, we use a Monte Carlo estimator of the score to define the regression target. This gradually shifts training toward the joint distribution of noisy samples and dual variables encountered by the sampler at inference time.

4 Convergence Analysis

The PDI algorithm defines a sampling process steered by a sequence of dual variables estimated via dual ascent. Because the multiplier changes along the trajectory, the marginal law p_t generated by PDI is generally not equal to $q_{T-t}(\cdot | \boldsymbol{\lambda}_t)$. The latter only defines the local fixed-multiplier score field used at that step. Thus, PDI is a path-dependent reverse process rather than the exact reversal of any single forward process in (6). We therefore analyze the convergence of the time-averaged dual iterates to a neighborhood of the optimal dual variable $\boldsymbol{\lambda}^*$. We then analyze how the residual errors in the multipliers and score fields propagate through the reverse dynamics and affect the terminal law p_T .

Theorem 1 (Convergence of time-average dual variables). *Let $\eta_t = \kappa/\sqrt{T}, \forall t$. For a sequence of $\{\lambda_t\}$ generated by PDI, it holds under regularity Assumptions 2–4 and arbitrary $\delta > 0$ that:*

$$\mathbb{E}[\|\bar{\lambda} - \lambda^*\|^2] \leq \frac{2}{\vartheta} \mathbb{E}[D^* - g(\bar{\lambda})] \leq \mathcal{O}\left(\frac{1}{\sqrt{T}}\right) + \Delta_{\text{floor}}, \quad (10)$$

with $\Delta_{\text{floor}} = \frac{12L_f^2}{\vartheta^2 T} \sum_{t=0}^{T-1} \left(\epsilon_{\text{TW}}^2(t+1) + \frac{\sigma_{T-t}^4}{\bar{\alpha}_{T-t}^2} \epsilon_{\text{app}}^2(t+1) \right) + \frac{12L_h^2}{\vartheta^2} \left(1 + \frac{1}{\delta}\right) \epsilon_{\text{hist}}^2$, and where $\bar{\lambda} = \frac{1}{T} \sum_t \lambda_t$ is the time-average of the multipliers, $g(\lambda) = \mathcal{L}(\mu_\lambda^\dagger, \lambda)$ is the dual function with strong concavity index ϑ , $\bar{\alpha}_{T-t} = \max\{\alpha_{\min}, \alpha_{T-t}\}$, and L_f, L_h are Lipschitz constants.

The assumptions and proof are provided in Appendix C.2. The theorem shows that the time-average of the dual variable converges at a rate of $1/\sqrt{T}$ to a region around the dual optimum. The floor arises from three error sources. The first is the Tweedie posterior-mean error $\epsilon_{\text{TW}}(t)$, which results from evaluating constraint violations on Tweedie posterior means rather than on clean samples from the current Gibbs distribution. The second is the score-approximation error, $\epsilon_{\text{app}}(t)$, which measures how errors in the learned score affect the Tweedie estimate. The third is the trajectory-history mismatch, ϵ_{hist} , which captures how past score-approximation errors propagate through the reverse process. Empirically, the score-approximation terms appear negligible. The dominant residual bias is therefore the Tweedie term. Its effect decreases toward the data side because the SNR increases, making the posterior mean estimate of the clean sample more accurate and reducing the bias in the dual update.

Since the dual variable parametrizes the Gibbs target, this implies that the time-averaged multiplier $\bar{\lambda}$ defines a near-optimal Gibbs target. A fresh fixed-multiplier sampler using $\bar{\lambda}$ across all diffusion steps would then target this distribution.

Dual convergence alone does not control the generated samples, because errors in λ_t enter the reverse dynamics through the score field and may be amplified by later kernels. We therefore quantify the stability of these reverse kernels. For a fixed multiplier λ , let K_t^λ denote the Markov kernel of the one-step reverse update in (7) using the score field $\nabla \log q_{T-t}(\cdot|\lambda)$. For any input law ν , the measure νK_t^λ denotes the law obtained by propagating ν through the one-step reverse kernel K_t^λ .

Proposition 2 (W_2 stability of the optimal kernel). *Let $K_t^{\lambda^*}$ be the Markov kernel of a reverse step (7) under the frozen optimal multiplier λ^* and the true score $\nabla \log q_{T-t}(\cdot|\lambda^*)$. Under Assumption 5, for all $\nu, \mu \in \mathcal{P}_2(\mathcal{X})$, it holds that*

$$W_2(\nu K_t^{\lambda^*}, \mu K_t^{\lambda^*}) \leq \rho_t W_2(\nu, \mu), \quad (11)$$

with $\rho_t = \frac{1}{\sqrt{a_{T-t}}} \sup_{\mathbf{x} \in \mathcal{X}} \|\mathbf{I} + b_{T-t} \nabla_{\mathbf{x}}^2 \log q_{T-t}(\mathbf{x}|\lambda^*)\|_{\text{op}}$.

The proof is provided in Appendix C.5. The coefficient ρ_t measures how stable one reverse step is and depends on the noise level. At high noise, the score field varies slowly and the reverse step is typically stable, i.e., $\rho_t < 1$. At medium noise, ρ_t is usually expected to remain moderate, although not necessarily smaller than one. Near the data side, the distribution becomes sharper and the score field can vary rapidly around the data manifold, so ρ_t may become larger and small errors can be amplified. Based on this kernel stability, we characterize the W_2 distance between the terminal and optimal distributions.

Theorem 2. *Under Assumptions 2, 4 and 5, the Wasserstein distance between the terminal distribution of PDI and the optimal distribution is controlled by the dual mismatch:*

$$\mathbb{E}[W_2(p_T, \mu^*)] \leq \sum_{t=0}^{T-1} \Psi_{t,T} \frac{b_{T-t}}{\sqrt{a_{T-t}}} \left(\gamma_t \mathbb{E}[\|\lambda_t - \lambda^*\|] + \epsilon_{\text{app}}(t) \right), \quad (12)$$

where $\Psi_{s,T} = \prod_{t=s+1}^T \rho_t$, and $\gamma_t = \frac{R\alpha_{T-t}}{\beta\sigma_{T-t}^2} \sqrt{\sup_{\lambda} \|\text{Cov}_{\pi_t}(\mathbf{y}_0|\mathbf{x}, \lambda)\|_{\text{op}}}$.

The proof is in Appendix C.3. The theorem shows that a dual mismatch at time t affects the final distribution through the future stability product $\prod_{s=t+1}^T \rho_s$. This product is controlled by the noise schedule. Keeping the SNR low for enough reverse steps keeps the score field smooth and the kernels more contractive, so early dual errors are damped rather than amplified. This provides a stable phase in which the dual variable can approach a neighborhood of λ^* . Later, when the SNR increases and the reverse dynamics become more sensitive, the remaining mismatch is already small. Empirically, we find that standard DDPM linear and cosine schedules provide this behavior.

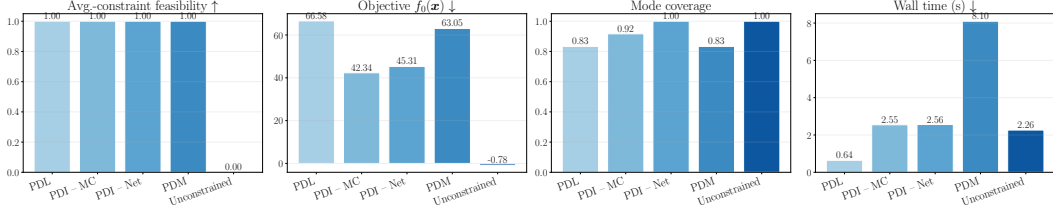


Figure 2: **Mixture of Gaussians** ($K = 12$ modes with $M = 10$ constraints in a 30-dimensional space). While PDI, PDL and PDM maintain full feasibility, PDI exhibits the best objective and mode diversity.

5 Numerical Results

We provide numerical evidence in three stochastic optimization problems: constrained MoG, wireless resource allocation, and portfolio management. More details are provided in Appendices E, F, and G.

5.1 Mixture of Gaussians

We first evaluate our approach on sampling from a weighted mixture of Gaussians in \mathbb{R}^d , $f_0(\mathbf{x}) = -\log \sum_{k=1}^K w_k \mathcal{N}(\mathbf{x}; \boldsymbol{\mu}_k, \boldsymbol{\Sigma}_k)$, truncated to a polytope $\{\mathbf{x} : \mathbf{A}^\top \mathbf{x} \preceq \mathbf{b}\}$. The optimization problem is

$$P_{\text{MoG}}^* = \min_{\mu(\mathbf{x})} \mathbb{E}_{\mathbf{x} \sim \mu} [f_0(\mathbf{x})] - \beta \mathcal{H}(\mu) \quad \text{s.t.} \quad \mathbb{E}_{\mathbf{x} \sim \mu} [\mathbf{A}^\top \mathbf{x} - \mathbf{b}] \preceq \mathbf{0}, \quad (13)$$

i.e., the sampler must produce a distribution that concentrates on high-density regions of the mixture while satisfying M linear inequality constraints in expectation.

Baselines. We compare our approach to two baselines: i) a projected diffusion model (PDM) [25], and ii) primal-dual Langevin (PDL) dynamics [27]. For PDM, we reuse our trained model with $\boldsymbol{\lambda} = \mathbf{0}$ as the base model that samples from the unconstrained MoG and performs a Cimmino parallel projection [29] onto the polytope at each time step.

Results. As shown in Figure 2, all constrained methods achieve the same constraint feasibility. However, our method (PDI-Net and PDI-MC) obtains a better objective value than the other constrained baselines. This is because the two baselines enforce the constraints on every generated sample, whereas our formulation only requires the constraints to hold in expectation. Pointwise enforcement is therefore more conservative and can discard useful samples for optimality that violate the constraints individually but could be offset by other samples in the distribution. We also include an ablation on the dual variable through the unconstrained baseline, which runs our model with $\boldsymbol{\lambda}$ fixed to zero at all time steps. As the figure shows, the unconstrained model ignores the constraints entirely and achieves the lowest objective. This performance confirms that the constrained behavior is not merely a consequence of the training algorithm.

5.2 Wireless Resource Allocation

For a given network state \mathbf{H} with $N = 200$ users, the goal is to maximize the ergodic sum-rate while satisfying a minimum ergodic rate constraint for each user. That is,

$$P_{\text{pc}}^* = \max_{\mu(\mathbf{x})} \mathbf{1}^\top \mathbf{r}(\mu, \mathbf{H}) + \beta \mathcal{H}(\mu), \quad \text{s.t.} \quad \mathbf{r}(\mu, \mathbf{H}) \geq \mathbf{1} \cdot r_{\min}, \quad (14)$$

where μ denotes the distribution of power allocations, and r_{\min} is the minimum ergodic rate requirement. The optimal solution is rarely a degenerate policy. Since users compete for the communication channels and cause interference, activating all users simultaneously is typically suboptimal and may prevent the rate constraints from being satisfied. Instead, the optimal distribution often corresponds to a multimodal switching policy, in which different subsets of users transmit at different times while meeting their rate requirements in expectation.

Baselines. In addition to PDL and PDM, we include two other diffusion-based baselines: i) diffusion posterior sampling (DPS) [28], and ii) supervised training (ST) with expert data [30]. The expert data are generated by a primal-dual method run for the deterministic version of (14) and its resulting trajectories (after a transient period) are collected to train the diffusion model.

Results. Table 1 shows that PDI achieves the best overall balance between mean rates (objective) and feasibility represented by the 5th-percentile rate and mean and sum violations. The 1st-percentile

Table 1: **Baseline comparisons.** PDI achieves a near-feasible performance and provides the best balance between mean rates and constraint violations in the wireless power allocation problem ($r_{\min} = 0.6$).

Method	Mean rates (\uparrow)	5th%ile rate (\uparrow)	1st%ile rate (\uparrow)	Mean viol. (\downarrow)	Sum viol. (\downarrow)	Feas. % (\uparrow)
Unconstrained	2.957 ± 0.123	0.239 ± 0.052	0.081 ± 0.037	0.0421 ± 0.0078	8.43 ± 1.57	85.6 ± 2.4
PDI-Net	2.803 ± 0.132	0.613 ± 0.042	0.424 ± 0.082	0.0062 ± 0.0027	1.25 ± 0.54	95.5 ± 1.5
PDI-Net (warm-up)	2.578 ± 0.132	0.670 ± 0.055	0.429 ± 0.102	0.0056 ± 0.0026	1.12 ± 0.51	96.7 ± 1.4
PDI-MC	2.839 ± 0.130	0.614 ± 0.052	0.355 ± 0.120	0.0085 ± 0.0037	1.71 ± 0.75	95.5 ± 1.5
PDL [27]	2.635 ± 0.141	0.641 ± 0.057	0.405 ± 0.106	0.0068 ± 0.0031	1.36 ± 0.63	96.2 ± 1.5
PDM [25]	2.591 ± 0.157	0.510 ± 0.082	0.165 ± 0.107	0.0180 ± 0.0065	3.61 ± 1.29	91.9 ± 2.7
DPS [28]	2.731 ± 0.138	0.461 ± 0.071	0.184 ± 0.082	0.0198 ± 0.0060	3.96 ± 1.19	90.8 ± 2.5
ST [30]	2.482 ± 0.134	0.825 ± 0.060	0.666 ± 0.071	0.0007 ± 0.0008	0.14 ± 0.16	99.3 ± 0.6

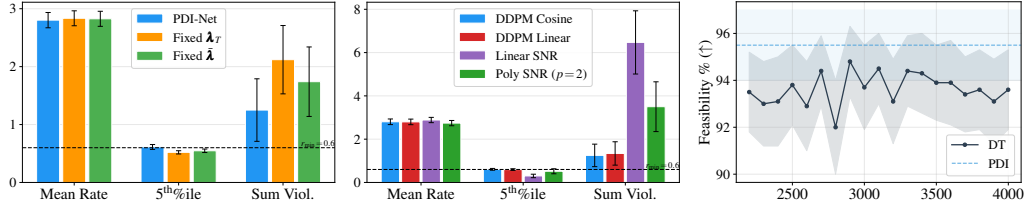


Figure 3: **Ablation.** Comparisons between our base PDI-Net model, plotted in blue, and (left) a PDI-Net while setting λ_t to a fixed value along the denoising trajectory, (middle) a PDI-Net with different noise schedules, and (right) DT checkpoints corresponding to different training epochs and different estimates of the dual variable.

users, however, are harder to correct by the dual variables and suffer under all methods, except for ST. Similarly to the MoG experiment, PDL and PDM achieve lower mean rates (worse objectives) with no substantial gains in feasibility because they sacrifice optimality for forcing pointwise constraints. Moreover, ST generates feasible solutions at the expense of optimality. Because ST is trained only to imitate expert trajectories, it is agnostic to the dual structure of the constrained distribution and cannot explicitly balance utility against feasibility during sampling. Lastly, instead of using the untrained score model to generate rollouts during the early epochs of training, we initialize these rollouts with the ST model. We observe that the trained PDI-Net with ST warm-up inherits the same bias toward feasibility, achieving a higher, feasible 1st-percentile rate. However, this comes at the expense of the objective value, which decreases from 2.80 to 2.58.

Ablation. Figure 3 (left) evaluates the effect of keeping the dual variable fixed during inference. We run the score model with two fixed values: the final dual iterate λ_T and the time-average dual variable $\bar{\lambda}$, both computed from our base experiment. The results suggest that the distribution generated by the full PDI dynamics is not equivalent to the Gibbs distribution associated with either fixed value. Instead, it behaves like a mixture induced by the changing dual variable, and this mixture exhibits better feasibility. Among the two values, the Gibbs distribution with $\bar{\lambda}$ provides a better approximation to the PDI-generated distribution than the one associated with the final iterate.

To evaluate the role of the noise schedule, we report the performance metrics of four schedules in Figure 3 (middle): the DDPM cosine used in our base experiment, the DDPM linear schedule and the linear and polynomial SNR schedules. The latter two schedules fail to generate feasible samples. This is because they move out of the low-SNR regime too quickly before the dual updates reduce the dual mismatch. As a result, in the high-SNR regime, when the stability factor ρ_t becomes larger than one, the reverse process amplifies the remaining mismatch, leading to large constraint violations.

Dual training. To ablate the role of inference-time dual updates, we train a score model $s_\phi(\mathbf{x}_t, t)$ that does not take the dual variable as input. During training, we still update the dual variables using a primal-dual algorithm, so the score model is trained against targets induced by the evolving dual variables. At inference, there are no more dual updates and the trained model therefore acts as a fixed sampling policy that is intended to sample from the optimal distributions. We refer to this approach as dual training (DT) and the training algorithm is provided in Appendix D.

Figures 3 (right) and 8 compare DT checkpoints along the training trajectory with PDI. Although some DT checkpoints reach dual variables close to those produced by PDI, their generated samples exhibit lower tail rates and lower feasibility. This indicates that matching the dual variables alone is not sufficient. Since DT does not condition the score model on the current multiplier, a checkpoint trained over a changing dual trajectory need not represent the score field associated with its current

Table 2: **Baseline comparison in portfolio management.** PDI provides the best tradeoff between return, entropy and risk.

Method	Mean return (\uparrow)	Feasibility (\uparrow)	Mean viol. (\downarrow)	N_{eff}	Entropy	$\lVert\text{Top1}\rVert$
PDI-Net	0.189 \pm 0.031	0.91 \pm 0.09	8.18e-07	16.3 \pm 2.0	4.57	151
PDI-MC	0.195 \pm 0.028	0.92 \pm 0.13	1.45e-04	15.9 \pm 8.4	5.23	240
PDL	0.165 \pm 0.013	0.96 \pm 0.03	8.50e-07	21.8 \pm 0.7	5.78	376
PDM	0.125 \pm 0.012	1.00 \pm 0.00	0.00e+00	63.2 \pm 13.0	3.88	100
DPS	0.333 \pm 0.048	0.70 \pm 0.04	4.29e-04	4.5 \pm 0.4	4.91	202
Unconstrained	0.477 \pm 0.121	0.76 \pm 0.04	1.95e-03	4.2 \pm 0.6	4.68	159

dual value. Instead, it reflects the accumulated effect of the preceding training trajectory. We further verify this in Appendix F.3 by freezing DT multipliers and continuing score training, which substantially improves performance but requires a much larger training budget. PDI avoids this limitation by keeping the dual variable as an explicit state during inference. Thus, when the dual update increases the penalty on violated constraints, the penalty is reflected directly in the denoising dynamics.

Out-of-distribution constraints. The dual state conditioning in our PDI score model also benefits OOD performance. In Figure 4, we plot the sum violation and feasibility percentage under different constraint levels r_{\min} , with $r_{\min} = 0.6$ corresponding to the in-distribution setting. We observe that PDI is more robust to the shift in r_{\min} . This is because the score function $\nabla \log q_{T-t}(\mathbf{x}_t | \boldsymbol{\lambda}_t)$ does not depend on r_{\min} directly. Instead, changing r_{\min} changes the constraint residual and, therefore, induces a different trajectory of dual variables. Since PDI is trained with both exploitation and exploration over $\boldsymbol{\lambda}$, the score model learns a family of score fields over a range of in-distribution dual values. Thus, as long as the dual trajectory induced by the new r_{\min} remains close to this learned range, PDI can adapt to the new OOD constraints.

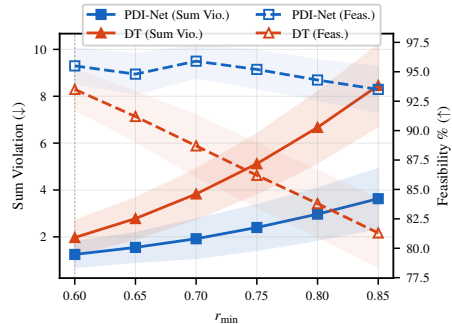


Figure 4: **Out-of-distribution constraints.** The models are trained under $r_{\min} = 0.6$ and tested under different values of constraint levels. PDI degrades more gracefully than DT, showing more robustness to distribution shifts.

5.3 Portfolio Management

In constrained portfolio optimization, we aim to allocate weights $\mathbf{x} \in \Delta^{N-1}$, where Δ^{N-1} is the $(N - 1)$ -dimensional probability simplex, across $N = 500$ assets, organized in 10 sectors. The return \mathbf{r} is drawn from a factor model with mean $\boldsymbol{\mu}$ and block-diagonal covariance $\boldsymbol{\Sigma}$. Our objective is to maximize expected return subject to per-asset variance-risk budgets, i.e.,

$$P_{\text{pm}}^* = \max_{\boldsymbol{\mu}(\mathbf{x})} \mathbb{E}_{\mathbf{x} \sim \boldsymbol{\mu}} [\mathbb{E}_{\mathbf{r}} [\mathbf{r}^\top \mathbf{x}]] + \beta \mathcal{H}(\boldsymbol{\mu}) \quad \text{s.t.} \quad \mathbb{E}_{\mathbf{x} \sim \boldsymbol{\mu}} [x_j (\boldsymbol{\Sigma} \mathbf{x})_j] \leq b_j, \quad j \in [N]. \quad (15)$$

The budget $b_j > 0$ caps how much variance asset j is permitted to contribute in expectation over all portfolios. The average constraints allow the sampler to trade risk across different portfolio samples, admitting occasional high-risk, high-return allocations while ensuring that the overall exposure of each asset remains within its prescribed budget in expectation.

Results. Table 2 shows that PDI achieves the best tradeoff between return, feasibility, and diversification among all diffusion samplers. The unconstrained model and DPS achieve higher returns, but only by incurring larger constraint violations and lower feasibility. In contrast, PDM and PDL are more feasible but more conservative, leading to lower returns. PDI lies between these extremes. It maintains high feasibility and very small mean violations while achieving the highest return among the feasible diffusion-based methods. Additional ablations in Appendix G confirm the same observations in the wireless allocation problem. That is, freezing the final or time-averaged multiplier underperforms the full PDI dynamics, and the noise schedule controls feasibility in a manner consistent with our stability analysis.

6 Conclusions

We introduced a primal–dual inference (PDI) framework that enforces distributional constraints by coupling a reverse diffusion process with dual ascent dynamics. We trained a single dual-variable-conditioned score network that serves the entire family of Gibbs targets encountered along the dual trajectory. At inference, PDI generates samples through a path-dependent sequence of Gibbs score fields indexed by the evolving multipliers, avoiding the need to first estimate and freeze an optimal dual variable. We analyzed PDI through the convergence of time-averaged dual iterates and a stability bound that quantifies how residual dual mismatch propagates through the reverse process. We validated our framework and methodology on constrained Gaussian sampling, wireless power control, and portfolio management. Extending PDI to adaptive dual step sizes, chance-constrained problems, and larger-scale setups are promising directions for future work. Our work has some limitations worth noting. The convergence guarantees of our algorithm apply to time-averaged dual iterates rather than final iterates or the primal distributions directly. Additionally, PDI requires problem-specific tuning of the dual-variable prior used during training and the entropy regularization strength β , for which principled selection rules remain an open question. Our code is available at: <https://github.com/SMRhadou/PDI-Diffusion>.

References

- [1] J. Sohl-Dickstein, E. Weiss, N. Maheswaranathan, and S. Ganguli, “Deep unsupervised learning using nonequilibrium thermodynamics,” in *Proceedings of the 32nd International Conference on Machine Learning* (F. Bach and D. Blei, eds.), vol. 37 of *Proceedings of Machine Learning Research*, (Lille, France), pp. 2256–2265, PMLR, 07–09 Jul 2015.
- [2] J. Ho, A. Jain, and P. Abbeel, “Denoising diffusion probabilistic models,” *arXiv preprint arxiv:2006.11239*, 2020.
- [3] Y. Song, J. Sohl-Dickstein, D. P. Kingma, A. Kumar, S. Ermon, and B. Poole, “Score-based generative modeling through stochastic differential equations,” in *International Conference on Learning Representations*, 2021.
- [4] R. Rombach, A. Blattmann, D. Lorenz, P. Esser, and B. Ommer, “High-Resolution Image Synthesis with Latent Diffusion Models,” in *2022 IEEE/CVF Conference on Computer Vision and Pattern Recognition (CVPR)*, (Los Alamitos, CA, USA), pp. 10674–10685, IEEE Computer Society, June 2022.
- [5] Z. Kong, W. Ping, J. Huang, K. Zhao, and B. Catanzaro, “Diffwave: A versatile diffusion model for audio synthesis,” in *International Conference on Learning Representations*, 2021.
- [6] J. Ho, T. Salimans, A. Gritsenko, W. Chan, M. Norouzi, and D. Fleet, “Video diffusion models,” in *Advances in Neural Information Processing Systems* (S. Koyejo, S. Mohamed, A. Agarwal, D. Belgrave, K. Cho, and A. Oh, eds.), vol. 35, pp. 8633–8646, Curran Associates, Inc., 2022.
- [7] Y. B. Uslu, S. Hadou, S. S. Bidokhti, and A. Ribeiro, “Generative diffusion models for resource allocation in wireless networks,” in *2025 IEEE 10th International Workshop on Computational Advances in Multi-Sensor Adaptive Processing (CAMSAP)*, pp. 201–205, IEEE, 2025.
- [8] A. Babazadeh Darabi and S. Coleri, “Diffusion model based resource allocation strategy in ultra-reliable wireless networked control systems,” *IEEE Communications Letters*, vol. 29, no. 1, pp. 85–89, 2025.
- [9] N. Tiwari, “Generative diffusion model for risk-neutral derivative pricing,” 2026.
- [10] M. He, X. He, and X. Gao, “Factor-based conditional diffusion model for portfolio optimization,” in *NeurIPS 2025 Workshop: Generative AI in Finance*, 2025.
- [11] Q. Zhang and Y. Chen, “Path integral sampler: a stochastic control approach for sampling,” in *International Conference on Learning Representations*, 2022.
- [12] F. Vargas, W. S. Grathwohl, and A. Doucet, “Denoising diffusion samplers,” in *The Eleventh International Conference on Learning Representations*, 2023.
- [13] J. Berner, L. Richter, and K. Ullrich, “An optimal control perspective on diffusion-based generative modeling,” *Transactions on Machine Learning Research*, 2024.
- [14] L. Richter and J. Berner, “Improved sampling via learned diffusions,” in *The Twelfth International Conference on Learning Representations*, 2024.

- [15] S. Khalafi, D. Ding, and A. Ribeiro, “Constrained diffusion models via dual training,” *Advances in Neural Information Processing Systems*, vol. 37, pp. 26543–26576, 2024.
- [16] S. Khalafi, I. Hounie, D. Ding, and A. Ribeiro, “Composition and alignment of diffusion models using constrained learning,” *arXiv preprint arXiv:2508.19104*, 2025.
- [17] B. Efron, “Tweedie’s formula and selection bias,” *Journal of the American Statistical Association*, vol. 106, no. 496, pp. 1602–1614, 2011.
- [18] P. Dhariwal and A. Q. Nichol, “Diffusion models beat GANs on image synthesis,” in *Advances in Neural Information Processing Systems* (A. Beygelzimer, Y. Dauphin, P. Liang, and J. W. Vaughan, eds.), 2021.
- [19] J. Ho and T. Salimans, “Classifier-free diffusion guidance,” *arXiv preprint arXiv:2207.12598*, 2022.
- [20] A. Nichol, P. Dhariwal, A. Ramesh, P. Shyam, P. Mishkin, B. McGrew, I. Sutskever, and M. Chen, “Glide: Towards photorealistic image generation and editing with text-guided diffusion models,” 2022.
- [21] A. Lou and S. Ermon, “Reflected diffusion models,” in *International Conference on Machine Learning*, pp. 22675–22701, PMLR, 2023.
- [22] G.-H. Liu, T. Chen, E. Theodorou, and M. Tao, “Mirror diffusion models for constrained and watermarked generation,” *Advances in Neural Information Processing Systems*, vol. 36, pp. 42898–42917, 2023.
- [23] V. De Bortoli, E. Mathieu, M. Hutchinson, J. Thornton, Y. W. Teh, and A. Doucet, “Riemannian score-based generative modelling,” *Advances in neural information processing systems*, vol. 35, pp. 2406–2422, 2022.
- [24] N. Fishman, L. Klarner, E. Mathieu, M. Hutchinson, and V. De Bortoli, “Metropolis sampling for constrained diffusion models,” *Advances in Neural Information Processing Systems*, vol. 36, pp. 62296–62331, 2023.
- [25] J. K. Christopher, S. Baek, and F. Fioretto, “Constrained synthesis with projected diffusion models,” *Advances in Neural Information Processing Systems*, vol. 37, pp. 89307–89333, 2024.
- [26] W. Huang, Y. Jiang, T. Van Wouwe, and C. K. Liu, “Constrained diffusion with trust sampling,” *NeurIPS*, 2024.
- [27] L. F. Chamon, M. R. Karimi, and A. Korba, “Constrained sampling with primal-dual langevin monte carlo,” *Advances in Neural Information Processing Systems*, vol. 37, pp. 29285–29323, 2024.
- [28] H. Chung, J. Kim, M. T. Mccann, M. L. Klasky, and J. C. Ye, “Diffusion posterior sampling for general noisy inverse problems,” in *International Conference on Learning Representations (ICLR)*, 2023.
- [29] F. Sloboda, “A projection method of the cimmino type for linear algebraic systems,” *Parallel Computing*, vol. 17, no. 4, pp. 435–442, 1991.
- [30] Y. B. Uslu, S. Hadou, S. S. Bidokhti, and A. Ribeiro, “Graph signal diffusion models for wireless resource allocation,” 2026.
- [31] A. Hyvärinen and P. Dayan, “Estimation of non-normalized statistical models by score matching,” *Journal of Machine Learning Research*, vol. 6, no. 4, 2005.
- [32] Y. Song and S. Ermon, “Generative modeling by estimating gradients of the data distribution,” *Advances in neural information processing systems*, vol. 32, 2019.
- [33] J. Song, C. Meng, and S. Ermon, “Denoising diffusion implicit models,” in *International Conference on Learning Representations*, 2021.
- [34] A. Q. Nichol and P. Dhariwal, “Improved denoising diffusion probabilistic models,” in *International conference on machine learning*, pp. 8162–8171, PMLR, 2021.
- [35] C. Lu, Y. Zhou, F. Bao, J. Chen, C. Li, and J. Zhu, “Dpm-solver: A fast ode solver for diffusion probabilistic model sampling in around 10 steps,” *arXiv preprint arXiv:2206.00927*, 2022.
- [36] T. Karras, M. Aittala, T. Aila, and S. Laine, “Elucidating the design space of diffusion-based generative models,” in *Proc. NeurIPS*, 2022.

- [37] J. Chen, L. Richter, J. Berner, D. Blessing, G. Neumann, and A. Anandkumar, “Sequential controlled langevin diffusions,” 2024.
- [38] C. Domingo-Enrich, M. Drozdal, B. Karrer, and R. T. Chen, “Adjoint matching: Fine-tuning flow and diffusion generative models with memoryless stochastic optimal control,” *arXiv preprint arXiv:2409.08861*, 2024.
- [39] M. Sendera, M. Kim, S. Mittal, P. Lemos, L. Scimeca, J. Rector-Brooks, A. Adam, Y. Bengio, and N. Malkin, “Improved off-policy training of diffusion samplers,” *Advances in Neural Information Processing Systems*, vol. 37, pp. 81016–81045, 2024.
- [40] Y. Guo, H. Yuan, Y. Yang, M. Chen, and M. Wang, “Gradient guidance for diffusion models: An optimization perspective,” in *Advances in Neural Information Processing Systems* (A. Globerson, L. Mackey, D. Belgrave, A. Fan, U. Paquet, J. Tomczak, and C. Zhang, eds.), vol. 37, pp. 90736–90770, Curran Associates, Inc., 2024.
- [41] L. Kong, Y. Du, W. Mu, K. Neklyudov, V. D. Bortoli, D. Wu, H. Wang, A. Ferber, Y.-A. Ma, C. P. Gomes, and C. Zhang, “Diffusion models as constrained samplers for optimization with unknown constraints,” 2025.
- [42] K. Black, M. Janner, Y. Du, I. Kostrikov, and S. Levine, “Training diffusion models with reinforcement learning,” in *The Twelfth International Conference on Learning Representations*, 2024.
- [43] Z. Sun and Y. Yang, “DIFUSCO: Graph-based diffusion solvers for combinatorial optimization,” in *Thirty-seventh Conference on Neural Information Processing Systems*, 2023.
- [44] J. Wen and J. Yang, “Distributionally robust optimization via diffusion ambiguity modeling,” *arXiv preprint arXiv:2510.22757*, 2025.
- [45] L. Kong, H. Wang, Y. Pan, C. W. Kim, M. Song, A. Nguyen, T. Wang, H. Xu, and M. Tambe, “Robust optimization with diffusion models for green security,” in *Proceedings of the Forty-first Conference on Uncertainty in Artificial Intelligence* (S. Chiappa and S. Magliacane, eds.), vol. 286 of *Proceedings of Machine Learning Research*, pp. 2325–2344, PMLR, 21–25 Jul 2025.
- [46] Z. Guo, W. Tang, and R. Xu, “Conditional diffusion guidance under hard constraint: A stochastic analysis approach,” *arXiv preprint arXiv:2602.05533*, 2026.
- [47] M. Arvinte and J. I. Tamir, “Mimo channel estimation using score-based generative models,” *IEEE Transactions on Wireless Communications*, vol. 22, no. 6, pp. 3698–3713, 2023.
- [48] N. Zilberstein, A. Swami, and S. Segarra, “Joint channel estimation and data detection in massive mimo systems based on diffusion models,” in *ICASSP 2024 - 2024 IEEE International Conference on Acoustics, Speech and Signal Processing (ICASSP)*, pp. 13291–13295, 2024.
- [49] Z. He, F. Héliot, and Y. Ma, “Deterministic score-based diffusion model for channel estimation in ris-assisted mimo systems,” in *2025 IEEE 26th International Workshop on Signal Processing and Artificial Intelligence for Wireless Communications (SPAWC)*, pp. 1–5, 2025.
- [50] T. Lee, J. Park, H. Kim, and J. G. Andrews, “Generating high dimensional user-specific wireless channels using diffusion models,” *IEEE Transactions on Wireless Communications*, vol. 25, pp. 2907–2921, 2026.
- [51] S. K. Ankireddy, H. Kim, and H. Kim, “Residual diffusion models for joint source channel coding of mimo csi,” in *2025 59th Asilomar Conference on Signals, Systems, and Computers*, pp. 55–62, IEEE, 2025.
- [52] H. Kim, T. Lee, H. Kim, G. De Veciana, M. A. Arfaoui, A. Koc, P. Pietraski, G. Zhang, and J. Kaewell, “Generative diffusion model-based compression of mimo csi,” in *ICC 2025 - IEEE International Conference on Communications*, pp. 6323–6328, 2025.
- [53] J. Guo, X. Xu, Y. Liu, and A. Nallanathan, “Diffusion model for multiple antenna communication,” *IEEE Communications Magazine*, vol. 63, no. 10, pp. 44–50, 2025.
- [54] T. Hui, X. Tang, Y. Wang, Q. Du, D. Niyato, and Z. Han, “Channel-aware conditional diffusion model for secure mu-miso communications,” *IEEE Transactions on Vehicular Technology*, p. 1–6, 2026.
- [55] X. Zhang and J. Yu, “Improve the training efficiency of drl for wireless communication resource allocation: The role of generative diffusion models,” *IEEE Transactions on Wireless Communications*, vol. 25, pp. 11593–11608, 2026.

- [56] T. Takahashi and T. Mizuno, "Generation of synthetic financial time series by diffusion models," *Quantitative Finance*, vol. 25, no. 10, pp. 1507–1516, 2025.
- [57] H. Choudhary, A. Orra, and M. Thakur, "Diffusion-augmented reinforcement learning for robust portfolio optimization under stress scenarios," 2025.
- [58] C. Jin and A. Agarwal, "Forecasting implied volatility surface with generative diffusion models," 2025.
- [59] T. Akhound-Sadegh, J. Rector-Brooks, A. J. Bose, S. Mittal, P. Lemos, C.-H. Liu, M. Sendera, S. Ravanbakhsh, G. Gidel, Y. Bengio, N. Malkin, and A. Tong, "Iterated denoising energy matching for sampling from Boltzmann densities," in *International Conference on Machine Learning (ICML)*, 2024.
- [60] Y. B. Uslu, N. NaderiAlizadeh, M. Eisen, and A. Ribeiro, "Fast state-augmented learning for wireless resource allocation with dual variable regression," 2025.

A Extended Related Work

Diffusion models and score-based generative modeling. Score-based diffusion models learn a stochastic reversal of a progressive noising process by matching the gradients of the log-density $\nabla_x \log p(x)$, a.k.a. the score function, for noisy observations [31]. Noise-conditional score networks [32] train a single network across noise levels and sample via annealed Langevin dynamics, while denoising diffusion probabilistic models [2] frame generation as iterative Gaussian denoising guided by a simplified ELBO. These formulations are unified in [3] as instances of a common SDE, whose time reversal yields a generative process; and admits an equivalent deterministic probability-flow ODE that enables exact likelihood computation and has motivated accelerated sampling schemes such as denoising diffusion implicit models (DDIMs) [33, 34, 35, 36].

Energy-based models and sampling from Gibbs targets. Energy-based models define distributions of the form $p(x) \propto \exp(-E(x))$, whose normalizing constant is generally intractable. Score-based methods sidestep this because the score $\nabla_x \log p(x) = -\nabla_x E(x)$ is independent of this constant. This has motivated the use of diffusion as a sampler from unnormalized Gibbs targets by learning a controlled SDE, whose terminal law matches the target, e.g., [11, 12, 13, 14, 37, 38, 39]. In our setting, the Lagrangian minimizers are also Gibbs distributions whose energies are linear in the dual variables. Crucially, the energies are not fixed as they evolve during inference through dual ascent. Furthermore, the score network is trained over a distribution of dual variables, or equivalently, a distribution of target energies, rather than for a single one.

Guided and constrained diffusion sampling. Guidance techniques steer reverse diffusion processes toward improved fidelity or reward/constraint alignment more generally. They do so by modifying the score entering Tweedie’s denoising formula [17], which expresses the MMSE-estimate of a clean signal (posterior mean) given a noisy signal observation in terms of the score function. Notably, classifier guidance [18] perturbs the predicted score with the gradient of a noise-aware classifier, trading diversity for fidelity. Classifier-free guidance [19] removes the external classifier, instead interpolating between conditional and unconditional modes of a shared model during inference. Subsequent variants, such as CLIP-based guidance [20], underpin most state-of-the-art diffusion systems.

Beyond guidance, an extensive body of work enforces domain-feasibility constraints on the diffusion process directly, e.g., boundary reflections [21], mirror diffusion [22], Riemannian score-based models [23], and log-barrier constructions [24]. A separate line of works target constraint-aware inference. In [25], projected diffusions that apply feasibility projections after each denoising step are proposed, while a trust sampling approach [26] reformulates each reverse step as a separate constrained optimization problem.

Closest to this paper are [15, 16, 27], which adopt a constrained learning formulation for average (expectation) constraints. Specifically, [15] shows that the optimal KL-constrained distribution is an entropy-tilted mixture of reference distributions, enforced through a primal–dual training scheme that pairs an outer-loop dual ascent with inner-loop Lagrangian score matching, with [16] extending this to reward-based alignment and product/mixture compositions. Primal–dual Langevin Monte Carlo (PD-LMC) [27] operates instead at sampling time and enforces equality and average constraints via gradient descent–ascent in Wasserstein space, without a learned generative model.

Our method shares the Lagrangian saddle-point structure of these works but differs in three key aspects: (i) the dual variable evolves jointly with the denoising trajectory rather than in a separate outer training loop [15, 16] or an ergodic Langevin chain (PD-LMC) [27], (ii) a score network is trained across a distribution of dual variables and conditioned on each dual variable, rather than refitting an unconditional score model per dual iterate, and (iii) the aggregation of samples along the dual-ascent path yields a robust mixture of primal distributions that realizes the entropy-regularized mixture structure of [15] – as well as the Gibbs targets of the energy-based sampling approaches discussed above – empirically at inference time rather than analytically at a single optimal multiplier.

Diffusion-enabled Stochastic Optimization. Pretrained diffusion models constrained on the data manifold can be steered toward downstream objectives through gradient-based guidance or fine-tuning [40], making them viable tools for learning-enabled optimization. Several works have exploited this connection between guidance with optimization gradients and regularized optimization.

[41] combined guided diffusion models and Langevin dynamics in a two-stage scheme that learns constrained samplers for optimization with unknown constraints. [42] reinterpreted the denoising chain as a multi-step Markov Decision Process (MDP) and applied policy-gradient methods to fine-tune diffusion models on non-differentiable rewards. Beyond continuous settings, diffusion models have also advanced combinatorial optimization [43], and distributionally robust optimization [44, 45, 46].

Diffusion models in wireless optimization and portfolio management. Diffusion models recast stochastic optimization as conditional sampling from learned solution distributions. This perspective is especially relevant to wireless communication systems, whose non-convex, constrained design problems typically admit optimal solutions that are probability distributions over optimization variables. E.g., [47, 48, 49] leveraged diffusion priors for score-based MIMO channel estimation, with subsequent works extending their use to CSI compression [50, 51, 52], beamforming design [53, 54], and resource allocation [55, 8, 7, 30]. Specifically for power control, [8] trains DDPMs to generate optimal allocations conditioned on the channel state, while [7, 30] proposes graph-signal diffusion models for matching primal-dual expert policies with near-optimal ergodic rates and cross-topology transferability.

Diffusion models have found great use in quantitative finance applications, where non-convex constraints and high-dimensional, heavy-tailed return distributions present analogous challenges to those encountered in wireless system design. E.g., [56] proposed wavelet-DDPMs for scenario and stylized facts generation. [57, 10] tackled robust portfolio management with conditional diffusion models, with [58, 9] enforcing arbitrage-free and risk-neutral diffusion dynamics for volatility forecasting.

B Proposed Algorithms

B.1 Score Network Training

We follow Algorithm 1 in training the score model $s_\theta(\mathbf{x}_t, t, \boldsymbol{\lambda}_t)$ using the regression loss in (9). To compute the true score for the pairs $(\mathbf{x}_t, \boldsymbol{\lambda}_t)$, we use an MC estimator of the score function of the Gibbs distribution, described in the following lemma.

Lemma 1 (MC estimator of the Gibbs score [59]). *For any \mathbf{y}_τ , the score function of the Gibbs distribution can be estimated by K_{MC} Monte Carlo samples as*

$$\nabla_{\mathbf{y}_\tau} \log q_\tau(\mathbf{y}_\tau | \boldsymbol{\lambda}) \approx \nabla_{\mathbf{y}_\tau} \log \frac{1}{K_{MC}} \sum_{k=1}^{K_{MC}} \exp \left(- E \left(\frac{\mathbf{y}_\tau + \sigma_\tau \boldsymbol{\epsilon}_k}{\alpha_\tau}, \boldsymbol{\lambda} \right) \right), \quad (16)$$

where $\boldsymbol{\epsilon}_k \sim \mathcal{N}(\mathbf{0}, \mathbf{I})$.

We refer the reader to [59] for the proof.

B.2 Inference Algorithm

At inference, we run multiple chains in parallel as described in Algorithm 2.

B.3 Practical Considerations

In training the score model, we combine exploitation and exploration to generate training pairs $(\mathbf{x}, \boldsymbol{\lambda})$. Exploitation is performed by rolling out the sampling process using the most recent score model and storing the resulting primal-dual trajectories in a replay buffer. These rollouts expose the model to the states and dual variables it is likely to encounter during inference. Exploration is introduced in two ways. First, we sample dual variables from a prior distribution to cover regions that may not be visited by the current rollouts. Second, we perturb both the primal and dual variables to improve robustness to local deviations from the replayed trajectories. The exploitation fraction $\rho_{\text{exp}}(n)$ controls the balance between replayed dual variables and prior-sampled dual variables throughout training.

Although we refer to the learned network as a score model, our implementation uses the noise-prediction parameterization. For each training pair $(\mathbf{x}_t, \boldsymbol{\lambda})$, the MC estimator computes the score of

Algorithm 1 Score Network Training

Require: Decay and noise schedule $a_{0:T}, b_{0:T}$, Perturbation params $(\rho_{\text{pert}}, \epsilon_x, \epsilon_\lambda)$, exploitation fraction $\rho_{\text{exp}}(n)$ for all n

- 1: Initialize replay buffer $\mathcal{B} \leftarrow \emptyset$, score network \mathbf{s}_θ
- 2: **for** $n = 1, \dots, N_{\text{outer}}$ **do**
- 3: **for** each problem \mathcal{G} in a batch $\mathcal{B}_{\text{train}}$ **do** ▷ Rollouts
- 4: Sample $\{\mathbf{x}_0^{(i)} \sim \mathcal{N}(\mathbf{0}, \mathbf{I})\}_i$, Initialize $\boldsymbol{\lambda} \leftarrow \boldsymbol{\lambda}_0$
- 5: Run inference (Algorithm 2) with \mathbf{s}_θ to obtain $\{(\mathbf{x}_t^{(i)}, t, \boldsymbol{\lambda}, \mathcal{G})\}_{t=0}^{T-1}, \forall i \in [I]$
- 6: Push $\{(\mathbf{x}_t^{(i)}, t, \boldsymbol{\lambda}, \mathcal{G})\}_i^I$ to \mathcal{B}
- 7: **end for**
- 8: **for** inner = $1, \dots, N_{\text{inner}}$ **do**
- 9: Sample a minibatch $\{(\mathbf{x}_t^{(j)}, t^{(j)}, \boldsymbol{\lambda}^{(j)}, \mathcal{G}^{(j)})\}_{j=1}^B$ from \mathcal{B}
- 10: **for** $j = 1, \dots, B$ **do**
- 11: **if** Bernoulli(ρ_{pert}) = 1 **then** ▷ Perturb training pairs
- 12: $\mathbf{x}_t^{(j)} \leftarrow \mathbf{x}_t^{(j)} + \epsilon_x \cdot \mathbf{z}_x, \quad \mathbf{z}_x \sim \mathcal{N}(\mathbf{0}, \mathbf{I})$
- 13: $\boldsymbol{\lambda}^{(j)} \leftarrow [\boldsymbol{\lambda}^{(j)} + \epsilon_\lambda \cdot \mathbf{z}_\lambda]_+, \quad \mathbf{z}_\lambda \sim \mathcal{N}(\mathbf{0}, \mathbf{I})$
- 14: **end if**
- 15: **if** Bernoulli($1 - \rho_{\text{exp}}(n)$) = 1 **then**
- 16: $\boldsymbol{\lambda}^{(j)} \leftarrow \mathbf{v}, \quad \mathbf{v} \sim \pi_{\text{prior}}(\cdot)$ ▷ Sample from a prior
- 17: **end if**
- 18: **end for**
- 19: $\boldsymbol{\theta} \leftarrow \boldsymbol{\theta} - \alpha \nabla \frac{1}{B} \sum_j w(t^{(j)}) \|\mathbf{s}_\theta(\mathbf{x}_t^{(j)}, t^{(j)}, \boldsymbol{\lambda}^{(j)}, \mathcal{G}^{(j)}) - \nabla \log q_{T-t^{(j)}}(\mathbf{x}_t^{(j)} \mid \boldsymbol{\lambda}^{(j)}; \mathcal{G}^{(j)})\|_2^2$
- 20: **end for**
- 21: **end for**
- 22: **return** $\boldsymbol{\theta}$

Algorithm 2 PDI Dynamics for a given problem instance \mathcal{G}

Require: Trained score network \mathbf{s}_{θ^*} , dual step size η_t , decay and noise schedule $a_{0:T}, b_{0:T}$

- 1: Initialize replay buffer $\mathcal{B} \leftarrow \emptyset$
- 2: **for** chain = $1, \dots, C$ **do**
- 3: Sample $\mathbf{x}_0^{(i)} \sim \mathcal{N}(\mathbf{0}, \mathbf{I}), \quad i = 1, \dots, I$ ▷ I i.i.d. samples
- 4: Initialize $\boldsymbol{\lambda} \leftarrow \boldsymbol{\lambda}_0$
- 5: **for** $t = 0, \dots, T - 1$ **do**
- 6: $\mathbf{x}_{t+1}^{(i)} = \frac{1}{\sqrt{\bar{\alpha}_{T-t}}} \left(\mathbf{x}_t^{(i)} + b_{T-t} \mathbf{s}_{\theta^*}(\mathbf{x}_t^{(i)}, t, \boldsymbol{\lambda}, \mathcal{G}) \right) + \sqrt{b_{T-t}} \mathbf{z}, \quad \mathbf{z} \sim \mathcal{N}(\mathbf{0}, \mathbf{I})$
- 7: $\hat{\mathbf{y}}_0^{(i)} \leftarrow (\mathbf{x}_{t+1}^{(i)} - \sigma_{T-t-1}^2 \mathbf{s}_{\theta^*}(\mathbf{x}_{t+1}^{(i)}, t+1, \boldsymbol{\lambda}, \mathcal{G})) / \bar{\alpha}_{T-t-1}$ ▷ Tweedie estimate
- 8: $\boldsymbol{\lambda} \leftarrow \left[\boldsymbol{\lambda} + \eta_t \cdot \sum_i \mathbf{f}(\hat{\mathbf{y}}_0^{(i)}) / I \right]_+$ ▷ Dual ascent
- 9: **end for**
- 10: Push $\{\mathbf{x}_T^{(i)}\}_i$ to \mathcal{B}
- 11: **end for**
- 12: **return** \mathcal{B}

the Gibbs distribution indexed by $\boldsymbol{\lambda}$ directly. Rather than regressing the network directly to this score, we reparameterize the target into the equivalent noise via $\boldsymbol{\epsilon}_t = -\sigma_{T-t} \mathbf{s}_t$, where \mathbf{s} is the MC score estimate. The network is therefore trained to predict this noise target. During sampling, the predicted noise is converted back into score units using the same relation, and the resulting score is used in the PDI reverse update. Thus, throughout the paper, training a score model should be understood as training a noise-prediction network whose target is derived from the same MC score estimate.

In some of our numerical examples, the samples must satisfy physical domain constraints, such as box constraints on transmit powers or simplex constraints on portfolio weights. We enforce these constraints by projecting the Tweedie estimate $\hat{\mathbf{y}}_0$ onto the corresponding domain immediately after Step 7 of Algorithm 2. We also ensure that we divide by $\bar{\alpha}_{T-t} = \max\{\alpha_{\min}, \alpha_{T-t}\}$ in computing the Tweedie to avoid numerical instabilities in the low-SNR regime.

C Analytical Proofs

The dual function of (1) is defined as

$$g(\boldsymbol{\lambda}) = \mathcal{L}(\mu_{\boldsymbol{\lambda}}^{\dagger}, \boldsymbol{\lambda}) = \min_{\mu \in \mathcal{P}_2(\mathcal{X})} \mathcal{L}(\mu, \boldsymbol{\lambda}), \quad (17)$$

where $\mu_{\boldsymbol{\lambda}}^{\dagger}$ is the Gibbs distribution induced by the dual variable $\boldsymbol{\lambda}$. We can then write the dual function in a closed form as

$$g(\boldsymbol{\lambda}) = \mathbb{E}_{\mu_{\boldsymbol{\lambda}}^{\dagger}} \left[f_0(\mathbf{x}) + \boldsymbol{\lambda}^{\top} \mathbf{f}(\mathbf{x}) \right] - \beta \mathcal{H}(\mu_{\boldsymbol{\lambda}}^{\dagger}) = -\beta \log Z(\boldsymbol{\lambda}). \quad (18)$$

The true gradient of the dual function is

$$\nabla g(\boldsymbol{\lambda}_t) = \mathbb{E}_{\mu_{\boldsymbol{\lambda}_t}^{\dagger}} [\mathbf{f}(\mathbf{y}_0)], \quad (19)$$

which is the violation estimated by clean samples of the distribution $\mu_{\boldsymbol{\lambda}_t}^{\dagger}$. PDI replaces this gradient with

$$\widehat{\nabla} g(\boldsymbol{\lambda}_t) = \mathbb{E}_{\mathbf{x}_{t+1} \sim p_{t+1}} \left[\mathbf{f} \left(\mathbb{E}_{\tilde{\pi}_{t+1}^{\theta}} [\mathbf{y}_0 | \mathbf{x}_{t+1}, \boldsymbol{\lambda}_t] \right) \right], \quad (20)$$

where p_t is the marginal distribution at time t and $\mathbb{E}_{\tilde{\pi}_{t+1}^{\theta}} [\mathbf{y}_0 | \mathbf{x}_{t+1}, \boldsymbol{\lambda}_t]$ is the Tweedie posterior mean under the score model \mathbf{s}_{θ} . This formula replaces clean samples with the Tweedie posterior means under the forward process started with $\mu_{\boldsymbol{\lambda}_t}^{\dagger}$. The bias in this gradient comes from three sources: i) replacing the score field with a parameterized network \mathbf{s}_{θ} , ii) propagating the dual mismatch and score-approximation error across diffusion steps (marginal mismatch), and iii) replacing clean samples \mathbf{y}_0 with a posterior mean $\mathbb{E}[\mathbf{y}_0 | \mathbf{x}_{t+1}, \boldsymbol{\lambda}_t]$ (Tweedie's error).

More concretely, we write the difference between the estimated gradient $\widehat{\nabla} g$ and true gradient ∇g as

$$\mathbf{b}_{t+1}(\boldsymbol{\lambda}_t) := \widehat{\nabla} g(\boldsymbol{\lambda}_t) - \nabla g(\boldsymbol{\lambda}_t) \quad (21)$$

$$= \mathbb{E}_{p_t} \left[\mathbf{f} \left(\mathbb{E}_{\tilde{\pi}_{t+1}^{\theta}} [\mathbf{y}_0 | \mathbf{x}_{t+1}, \boldsymbol{\lambda}_t] \right) \right] - \mathbb{E}_{\mu_{\boldsymbol{\lambda}_t}^{\dagger}} [\mathbf{f}(\mathbf{y}_0)] \quad (22)$$

$$= \mathbb{E}_{p_{t+1}} \left[\mathbf{f} \left(\mathbb{E}_{\tilde{\pi}_{t+1}^{\theta}} [\mathbf{y}_0 | \mathbf{x}_{t+1}, \boldsymbol{\lambda}_t] \right) \right] - \mathbb{E}_{p_{t+1}} \left[\mathbf{f} \left(\mathbb{E}_{\tilde{\pi}_{t+1}} [\mathbf{y}_0 | \mathbf{x}_{t+1}, \boldsymbol{\lambda}_t] \right) \right] \quad (23)$$

$$\begin{aligned} &+ \mathbb{E}_{p_{t+1}} \left[\mathbf{f} \left(\mathbb{E}_{\tilde{\pi}_{t+1}^{\theta}} [\mathbf{y}_0 | \mathbf{x}_{t+1}, \boldsymbol{\lambda}_t] \right) \right] - \mathbb{E}_{\tilde{p}_{t+1}} \left[\mathbf{f} \left(\mathbb{E}_{\tilde{\pi}_{t+1}} [\mathbf{y}_0 | \tilde{\mathbf{x}}_{t+1}, \boldsymbol{\lambda}_t] \right) \right] \\ &+ \mathbb{E}_{\tilde{p}_{t+1}} \left[\mathbf{f} \left(\mathbb{E}_{\tilde{\pi}_{t+1}} [\mathbf{y}_0 | \tilde{\mathbf{x}}_{t+1}, \boldsymbol{\lambda}_t] \right) \right] - \mathbb{E}_{\mu_{\boldsymbol{\lambda}_t}^{\dagger}} [\mathbf{f}(\mathbf{y}_0)]. \end{aligned} \quad (24)$$

We bound the norm of the three terms in Lemmas 3, 4 and 5 (Section C.4).

The bias in the gradient results in dual convergence with a small but irreducible floor error. Theorem 1 characterizes this floor error and shows that it is controlled by the expected Tweedie posterior-mean error and the approximation error of the parameterization. Theorem 2 then analyzes how the residual errors in the multipliers and score fields propagate through the reverse dynamics and affect the terminal law p_T . In Sections C.2 and C.3, we provide the analytical proofs of these theorems. The assumptions under which our analysis holds are listed in Section C.1.

C.1 Assumptions

Our proof holds under the following set of assumptions:

Assumption 2 (Constraint regularity). *The constraint function \mathbf{f} is L_f -Lipschitz, i.e., $\|\mathbf{f}(\mathbf{x}) - \mathbf{f}(\mathbf{y})\| \leq L_f \|\mathbf{x} - \mathbf{y}\|$. Also, the constraint function is bounded on the compact set \mathcal{X} , i.e., $\sup_{\mathbf{x} \in \mathcal{X}} \|\mathbf{f}(\mathbf{x})\| \leq R$.*

Assumption 3 (Strong dual concavity). *The dual function g is ϑ -strongly concave, i.e., $\nabla_{\boldsymbol{\lambda}}^2 g(\boldsymbol{\lambda}) \preceq -\vartheta \mathbf{I}$, for all $\boldsymbol{\lambda} \in \boldsymbol{\Lambda}$.*

The strong concavity modulus ϑ is not an independent quantity but is determined by the temperature β and the constraint covariance under the induced Gibbs-distribution family. Since the dual function is $g(\boldsymbol{\lambda}) = -\beta \log Z(\boldsymbol{\lambda})$, its Hessian is given by

$$\nabla^2 g(\boldsymbol{\lambda}) = -\frac{1}{\beta} \mathbf{Cov}_{\mu_{\boldsymbol{\lambda}}^{\dagger}} (\mathbf{f}(\mathbf{x})),$$

and $\vartheta = \frac{1}{\beta} \inf_{\lambda} \sigma_{\min}(\mathbf{Cov}_{\mu_{\lambda}^{\dagger}}(\mathbf{f}(\mathbf{x})))$, where σ_{\min} is the smallest eigenvalue of the covariance matrix. This makes Assumption 3 a mild and verifiable condition. The covariance of the constraints is strictly positive whenever the constraint covariance is nonsingular, and its smallest eigenvalue can be estimated directly from the samples generated during inference.

Assumption 4 (Rich parameterization). *For any function s_t , there exists a parameterization θ such that, uniformly over $\lambda \in \Lambda$, it holds that*

$$\mathbb{E}_{p_t, \mathcal{G}} \left[\left\| \mathbf{s}_{\theta}(\mathbf{x}_t, t, \lambda, \mathcal{G}) - s_t(\mathbf{x}_t | \lambda; \mathcal{G}) \right\|_2^2 \right] \leq \epsilon_{\text{app}}^2(t). \quad (25)$$

Assumption 4 is an approximation condition on the score network. We require it only uniformly over the compact set Λ in which the dual iterates evolve. The error $\epsilon_{\text{app}}^2(t)$ aggregates three sources: i) the finite expressivity of the parameterization, ii) the variance of the Monte Carlo score estimator (Lemma 1) used to form the regression targets, and iii) the mismatch between the rollout-induced training distribution of (\mathbf{x}_t, λ) pairs and the distribution encountered at inference. The expressivity of the parameterization controls the first source, and our training procedure is designed to control the latter two. That is, the exploration/exploitation rollout scheme with a replay buffer reduces the distribution shift, and K_{MC} candidates reduce the estimator variance. Our numerical experiments show that the difference between PDI with a trained score model (PDI-Net) and PDI with an MC score field (PDI-MC) is negligible. In some cases, PDI-Net improves PDI-MC on feasibility and tail-rate metrics.

Assumption 5. *Assume the noised optimal score is spatially Lipschitz, i.e. $\nabla_{\mathbf{x}}^2 \log q_{T-t}(\mathbf{x} | \lambda)$ exists and is bounded in operator norm, $\sup_{\mathbf{x} \in \mathcal{X}} \|\nabla_{\mathbf{x}}^2 \log q_{T-t}(\mathbf{x} | \lambda)\|_{\text{op}} \leq M_t$, for each t and $\lambda \in \Lambda$.*

C.2 Dual Convergence: Proof of Theorem 1

Proof. From Lemma 2, the dual recursion is

$$\begin{aligned} \mathbb{E}[\|\lambda_{t+1} - \lambda^*\|^2] + \eta \mathbb{E}[D^* - g(\lambda_t)] + 2\eta\beta \mathbb{E}[D_{\text{KL}}(\mu_{\lambda_t}^{\dagger} \| \mu^*)] \\ \leq \mathbb{E}[\|\lambda_t - \lambda^*\|^2] + \frac{2\eta}{\vartheta} \mathbb{E}[\|\mathbf{b}_{t+1}(\lambda_t)\|^2] + \eta^2 R^2. \end{aligned} \quad (26)$$

Using the telescope sum, we get

$$\begin{aligned} \mathbb{E}[\|\lambda_T - \lambda^*\|^2] + \eta \sum_{t=0}^{T-1} \mathbb{E}[D^* - g(\lambda_t)] + 2\eta\beta \sum_{t=0}^{T-1} \mathbb{E}[D_{\text{KL}}(\mu_{\lambda_t}^{\dagger} \| \mu^*)] \\ \leq \mathbb{E}[\|\lambda_0 - \lambda^*\|^2] + \frac{2\eta}{\vartheta} \sum_{t=0}^{T-1} \mathbb{E}[\|\mathbf{b}_{t+1}(\lambda_t)\|^2] + T\eta^2 R^2. \end{aligned} \quad (27)$$

The bias comprises three components as described in (24). The Tweedie posterior mean error is bounded by Lemma 3:

$$\mathbb{E}[\|B_1(t+1)\|^2] \leq L_f^2 \epsilon_{TW}^2(t+1). \quad (28)$$

The marginal mismatch error is bounded by Lemma 4:

$$\mathbb{E}[\|B_2(t+1)\|^2] \leq L_h^2 \left((1 + \delta) C_{\text{hist}}^2 \eta^2 R^2 + \left(1 + \frac{1}{\delta}\right) \epsilon_{\text{hist}}^2 \right). \quad (29)$$

Finally, the parameterization error is bounded by Lemma 5:

$$\mathbb{E}[\|B_3(t+1)\|^2] \leq L_f^2 \frac{\sigma_{T-t}^4}{\alpha_{T-t}^2} \epsilon_{\text{app}}^2(t+1). \quad (30)$$

The total bias can then be bounded as

$$\mathbb{E}[\|\mathbf{b}_{t+1}(\lambda_t)\|^2] \leq 3\mathbb{E}[\|B_1(t+1)\|^2] + 3\mathbb{E}[\|B_2(t+1)\|^2] + 3\mathbb{E}[\|B_3(t+1)\|^2] \quad (31)$$

$$\leq 3L_f^2 \epsilon_{TW}^2(t+1) + 3L_h^2 \left((1 + \delta) C_{\text{hist}}^2 \eta^2 R^2 + \left(1 + \frac{1}{\delta}\right) \epsilon_{\text{hist}}^2 \right) \quad (32)$$

$$+ 3L_f^2 \frac{\sigma_{T-t}^4}{\alpha_{T-t}^2} \epsilon_{\text{app}}^2(t+1). \quad (33)$$

Substituting the bias in (27), the RHS is

$$\mathcal{I} \leq \mathbb{E}[\|\boldsymbol{\lambda}_0 - \boldsymbol{\lambda}^*\|^2] + \frac{6L_f^2\eta}{\vartheta} \sum_{t=0}^{T-1} \epsilon_{TW}^2(t+1) + (1+\delta) \frac{6L_h^2\eta}{\vartheta} TC_{\text{hist}}^2 \eta^2 R^2 \quad (34)$$

$$+ \frac{6L_h^2\eta}{\vartheta} \left(1 + \frac{1}{\delta}\right) T \epsilon_{\text{hist}}^2 + \frac{6L_f^2\eta}{\vartheta} \sum_{t=0}^{T-1} \frac{\sigma_{T-t}^4}{\alpha_{T-t}^2} \epsilon_{\text{app}}^2(t+1) + T \eta^2 R^2. \quad (35)$$

Choose $\eta = \kappa/\sqrt{T}$. Since the left-side terms in (27) are non-negative, each one of them is bounded above by \mathcal{I} . Thus, we get a uniform average dual gap of

$$\frac{1}{T} \sum_{t=0}^{T-1} \mathbb{E}[D^* - g(\boldsymbol{\lambda}_t)] \leq \frac{\mathcal{I}}{\eta T} \quad (36)$$

$$\begin{aligned} &= \underbrace{\frac{\mathbb{E}[\|\boldsymbol{\lambda}_0 - \boldsymbol{\lambda}^*\|^2]}{\eta T}}_{\mathcal{O}\left(\frac{1}{\sqrt{T}}\right)} + \frac{6L_f^2}{\vartheta T} \sum_{t=0}^{T-1} \epsilon_{TW}^2(t+1) + (1+\delta) \underbrace{\frac{6L_h^2}{\vartheta T} C_{\text{hist}}^2 R^2 \eta^2}_{\mathcal{O}\left(\frac{1}{T}\right)} \\ &\quad + \frac{6L_h^2}{\vartheta} \left(1 + \frac{1}{\delta}\right) \epsilon_{\text{hist}}^2 + \frac{6L_f^2}{\vartheta T} \sum_{t=0}^{T-1} \frac{\sigma_{T-t}^4}{\alpha_{T-t}^2} \epsilon_{\text{app}}^2(t+1) + \underbrace{\eta R^2}_{\mathcal{O}\left(\frac{1}{\sqrt{T}}\right)} \end{aligned} \quad (37)$$

$$= \mathcal{O}\left(\frac{1}{\sqrt{T}}\right) + \frac{6L_f^2}{\vartheta T} \sum_{t=0}^{T-1} \left(\epsilon_{TW}^2(t+1) + \frac{\sigma_{T-t}^4}{\alpha_{T-t}^2} \epsilon_{\text{app}}^2(t+1)\right) + \frac{6L_h^2}{\vartheta} \left(1 + \frac{1}{\delta}\right) \epsilon_{\text{hist}}^2. \quad (38)$$

The rate of convergence of both quantities is $1/\sqrt{T}$ and they converge to a neighborhood determined by ϵ_{TW} and ϵ_{t+1} across diffusion steps.

Define the time-average dual variable $\bar{\boldsymbol{\lambda}} = \frac{1}{T} \sum_t \boldsymbol{\lambda}_t$. By concavity of g , we have

$$\mathbb{E}[D^* - g(\bar{\boldsymbol{\lambda}})] \leq \mathbb{E}\left[D^* - \frac{1}{T} \sum_{t=0}^{T-1} g(\boldsymbol{\lambda}_t)\right] = \frac{1}{T} \sum_{t=0}^{T-1} \mathbb{E}[D^* - g(\boldsymbol{\lambda}_t)], \quad (39)$$

which is bounded by (38). Furthermore, by the strong concavity of g , we can also write

$$\mathbb{E}[\|\bar{\boldsymbol{\lambda}} - \boldsymbol{\lambda}^*\|^2] \leq \frac{2}{\vartheta} \mathbb{E}[D^* - g(\bar{\boldsymbol{\lambda}})], \quad (40)$$

which completes the proof. \square

Lemma 2. *Under Assumptions 2 and 3, and with $\eta_t = \eta$, the distance between $\boldsymbol{\lambda}_t$ and the optimum in expectation is given by*

$$\begin{aligned} &\mathbb{E}[\|\boldsymbol{\lambda}_{t+1} - \boldsymbol{\lambda}^*\|^2] + \eta \mathbb{E}[D^* - g(\boldsymbol{\lambda}_t)] + 2\eta\beta \mathbb{E}[D_{KL}(\mu_{\boldsymbol{\lambda}_t}^\dagger \|\mu^*)]. \\ &\leq \mathbb{E}[\|\boldsymbol{\lambda}_t - \boldsymbol{\lambda}^*\|^2] + \frac{2\eta}{\vartheta} \mathbb{E}[\|\mathbf{b}_t\|^2] + \eta^2 R^2. \end{aligned} \quad (41)$$

Proof. By the non-expansive property of the projection operator onto \mathbb{R}_+^M , we have $\|[\boldsymbol{\lambda}]_+ - \boldsymbol{\lambda}^*\| \leq \|\boldsymbol{\lambda} - \boldsymbol{\lambda}^*\|$, and therefore,

$$\mathbb{E}[\|\boldsymbol{\lambda}_{t+1} - \boldsymbol{\lambda}^*\|^2 | \mathcal{F}_t] \leq \|\boldsymbol{\lambda}_t + \eta \widehat{\nabla} g(\boldsymbol{\lambda}_t) - \boldsymbol{\lambda}^*\|^2, \quad (42)$$

where \mathcal{F}_t is a filtration of the history of the PDI process till time t .

Define the true gradient of the dual function as

$$\nabla g(\boldsymbol{\lambda}_t) = \mathbb{E}_{\mu_{\boldsymbol{\lambda}_t}^\dagger}[\mathbf{f}(\mathbf{y}_0)],$$

which is the constraint violations evaluated on clean samples under the current Gibbs distribution $\mu_{\boldsymbol{\lambda}_t}^\dagger$. PDI replaces this true gradient with a biased one, $\widehat{\nabla} g(\boldsymbol{\lambda}_t)$, and the bias $\mathbf{b}_t(\boldsymbol{\lambda}_t)$ is split into three

terms, as characterized in (24). Thus, we can write

$$\mathbb{E}[\|\boldsymbol{\lambda}_{t+1} - \boldsymbol{\lambda}^*\|^2 | \mathcal{F}_t] \leq \|\boldsymbol{\lambda}_t + \eta \widehat{\nabla} g(\boldsymbol{\lambda}_t) - \boldsymbol{\lambda}^*\|^2 \quad (43)$$

$$\leq \|\boldsymbol{\lambda}_t - \boldsymbol{\lambda}^*\|^2 + 2\eta \langle \boldsymbol{\lambda}_t - \boldsymbol{\lambda}^*, \widehat{\nabla} g(\boldsymbol{\lambda}_t) \rangle + \eta^2 \|\widehat{\nabla} g(\boldsymbol{\lambda}_t)\|^2 \quad (44)$$

$$= \|\boldsymbol{\lambda}_t - \boldsymbol{\lambda}^*\|^2 + 2\eta \langle \boldsymbol{\lambda}_t - \boldsymbol{\lambda}^*, \nabla g(\boldsymbol{\lambda}_t) \rangle + 2\eta \langle \boldsymbol{\lambda}_t - \boldsymbol{\lambda}^*, \mathbf{b}_t(\boldsymbol{\lambda}_t) \rangle + \eta^2 \|\widehat{\nabla} g(\boldsymbol{\lambda}_t)\|^2. \quad (45)$$

By Lemma 8, the Lagrangian function can be written as

$$\mathcal{L}(\mu, \boldsymbol{\lambda}) = \beta D_{\text{KL}}(\mu \| \mu_{\boldsymbol{\lambda}}^\dagger) + g(\boldsymbol{\lambda}),$$

which leads to

$$\langle \boldsymbol{\lambda}_t - \boldsymbol{\lambda}^*, \nabla g(\boldsymbol{\lambda}_t) \rangle = \mathcal{L}(\mu_{\boldsymbol{\lambda}_t}^\dagger, \boldsymbol{\lambda}_t) - \mathcal{L}(\mu_{\boldsymbol{\lambda}_t}^\dagger, \boldsymbol{\lambda}^*) \quad (46)$$

$$= \underbrace{g(\boldsymbol{\lambda}_t) - g(\boldsymbol{\lambda}^*)}_{\text{duality gap}} - \beta D_{\text{KL}}(\mu_{\boldsymbol{\lambda}_t}^\dagger \| \mu^*). \quad (47)$$

The first equality follows from the definition in (2) and the second follows from the definition in the lemma. Using Young's inequality, for any $c > 0$, we can bound the inner product between $\boldsymbol{\lambda}_t - \boldsymbol{\lambda}^*$ and the bias by

$$2\langle \boldsymbol{\lambda}_t - \boldsymbol{\lambda}^*, \mathbf{b}_t^{(i)} \rangle \leq c \|\boldsymbol{\lambda}_t - \boldsymbol{\lambda}^*\|^2 + \frac{1}{c} \|\mathbf{b}_t^{(i)}\|^2. \quad (48)$$

Choose $c = \vartheta/2$. Thus, we get

$$\begin{aligned} \mathbb{E}[\|\boldsymbol{\lambda}_{t+1} - \boldsymbol{\lambda}^*\|^2 | \mathcal{F}_t] + 2\eta \left(g(\boldsymbol{\lambda}^*) - g(\boldsymbol{\lambda}_t) \right) + 2\eta \beta D_{\text{KL}}(\mu_{\boldsymbol{\lambda}_t}^\dagger \| \mu^*) \\ \leq \left(1 + \frac{\eta \vartheta}{2} \right) \|\boldsymbol{\lambda}_t - \boldsymbol{\lambda}^*\|^2 + \frac{2\eta}{\vartheta} \|\mathbf{b}_t\|^2 + \eta^2 \|\widehat{\nabla} g(\boldsymbol{\lambda}_t)\|^2. \end{aligned} \quad (49)$$

From the strong concavity of g (Assumption 3), we have $D^* - g(\boldsymbol{\lambda}_t) \geq \frac{\vartheta}{2} \|\boldsymbol{\lambda}_t - \boldsymbol{\lambda}^*\|^2$ with $D^* = g(\boldsymbol{\lambda}^*)$.

We then split the dual gap in the LHS into two halves and lower bound one of them with $\frac{\eta \vartheta}{2} \|\boldsymbol{\lambda}_t - \boldsymbol{\lambda}^*\|^2$. Thus, we have

$$\begin{aligned} \mathbb{E}[\|\boldsymbol{\lambda}_{t+1} - \boldsymbol{\lambda}^*\|^2 | \mathcal{F}_t] + \eta (D^* - g(\boldsymbol{\lambda}_t)) + 2\eta \beta D_{\text{KL}}(\mu_{\boldsymbol{\lambda}_t}^\dagger \| \mu^*) \\ \leq \|\boldsymbol{\lambda}_t - \boldsymbol{\lambda}^*\|^2 + \frac{2\eta}{\vartheta} \|\mathbf{b}_t^{(i)}\|^2 + \eta^2 \|\widehat{\nabla} g(\boldsymbol{\lambda}_t)\|^2. \end{aligned} \quad (50)$$

Take the expectation with respect to the filtration and bound the gradient with R (Assumption 2). This completes the proof. \square

C.3 Primal Recursion: Proof of Theorem 2

Proof. Let $K_t^{\boldsymbol{\lambda}_t}$ be the kernel of the parametrized PDI process, i.e., $p_{t+1} = p_t K_t^{\boldsymbol{\lambda}_t}$, and $K_t^{\boldsymbol{\lambda}^*}$ is its equivalent in the backward process with a fixed dual variable $\boldsymbol{\lambda}^*$ and the true score, i.e., $q_{T-t-1}^{\boldsymbol{\lambda}^*} = q_{T-t}^{\boldsymbol{\lambda}^*} K_t^{\boldsymbol{\lambda}^*}$. By the triangle inequality, we get

$$W_2(p_{t+1}, q_{T-t-1}^{\boldsymbol{\lambda}^*}) = W_2(p_t K_t^{\boldsymbol{\lambda}_t}, q_{T-t}^{\boldsymbol{\lambda}^*} K_t^{\boldsymbol{\lambda}^*}) \quad (51)$$

$$\leq W_2(p_t K_t^{\boldsymbol{\lambda}^*}, q_{T-t}^{\boldsymbol{\lambda}^*} K_t^{\boldsymbol{\lambda}^*}) + W_2(p_t K_t^{\boldsymbol{\lambda}_t}, p_t K_t^{\boldsymbol{\lambda}^*}). \quad (52)$$

The first term is bounded by (11) in Proposition 2, and the second term computes the effect of the mismatch in the dual variables.

Synchronous Coupling: We consider a synchronous coupling Π_t between $p_t K_t^{\boldsymbol{\lambda}_t}$ and $p_t K_t^{\boldsymbol{\lambda}^*}$ that shares the noise ϵ since the two kernels have the same noise covariance. Given a particle $\mathbf{x}_t \sim p_t$, the PDI kernel converts it into

$$\mathbf{x}_{t+1} = \frac{1}{\sqrt{a_\tau}} \left(\mathbf{x}_t + b_\tau \mathbf{s}_\theta(\mathbf{x}_t, t, \boldsymbol{\lambda}_t) \right) + \sqrt{b_\tau} \epsilon, \quad (53)$$

where $\tau = T - t$, while the optimal kernel transports it into

$$\tilde{\mathbf{x}}_{t+1} = \frac{1}{\sqrt{a_\tau}} \left(\mathbf{x}_t + b_\tau \mathbf{s}_t(\mathbf{x}_t | \boldsymbol{\lambda}^*) \right) + \sqrt{b_\tau} \boldsymbol{\epsilon}, \quad (54)$$

where $\mathbf{s}_t = \nabla \log q_{T-t}$ is the true score and \mathbf{s}_θ is the parameterized score function. By construction, Π_t is a valid coupling.

Bounding the W_2 distance then reduces to bounding the norm of the difference between the score functions under two different dual variables. More concretely, we have

$$\|\mathbf{x}_{t+1} - \tilde{\mathbf{x}}_{t+1}\| = \frac{b_\tau}{\sqrt{a_\tau}} \|\mathbf{s}_\theta(\mathbf{x}_t, t, \boldsymbol{\lambda}_t) - \mathbf{s}_t(\mathbf{x}_t | \boldsymbol{\lambda}^*)\| \quad (55)$$

$$\leq \frac{b_\tau}{\sqrt{a_\tau}} \left(\|\mathbf{s}_\theta(\mathbf{x}_t, t, \boldsymbol{\lambda}_t) - \mathbf{s}_t(\mathbf{x}_t | \boldsymbol{\lambda}_t)\| + \|\mathbf{s}_t(\mathbf{x}_t | \boldsymbol{\lambda}_t) - \mathbf{s}_t(\mathbf{x}_t | \boldsymbol{\lambda}^*)\| \right). \quad (56)$$

By Lemma 7, we have

$$\|\mathbf{s}_t(\mathbf{x}_t | \boldsymbol{\lambda}_t) - \mathbf{s}_t(\mathbf{x}_t | \boldsymbol{\lambda}^*)\| \leq \gamma_t \|\boldsymbol{\lambda}_t - \boldsymbol{\lambda}^*\|. \quad (57)$$

Combined with Assumption 4, we can bound the dual mismatch with

$$W_2(p_t K_t^{\boldsymbol{\lambda}_t}, p_t K_t^{\boldsymbol{\lambda}^*}) = \left(\inf_{\pi} \int \|\mathbf{x}_{t+1} - \tilde{\mathbf{x}}_{t+1}\|^2 d\pi(\mathbf{x}_{t+1}, \tilde{\mathbf{x}}_{t+1}) \right)^{1/2} \quad (58)$$

$$\leq \left(\int \|\mathbf{x}_{t+1} - \tilde{\mathbf{x}}_{t+1}\|^2 d\Pi_t(\mathbf{x}_{t+1}, \tilde{\mathbf{x}}_{t+1}) \right)^{1/2} \quad (59)$$

$$\leq \frac{b_\tau}{\sqrt{a_\tau}} (\gamma_t \|\boldsymbol{\lambda}_t - \boldsymbol{\lambda}^*\| + \epsilon_{\text{app}}(t)), \quad (60)$$

where the last inequality follows by Minkowski inequality. Substituting in (52), we get

$$W_2(p_{t+1}, q_{T-t-1}^{\boldsymbol{\lambda}^*}) \leq \rho_t W_2(p_t, q_{T-t}^{\boldsymbol{\lambda}^*}) + \frac{b_\tau}{\sqrt{a_\tau}} \gamma_t \|\boldsymbol{\lambda}_t - \boldsymbol{\lambda}^*\| + \frac{b_\tau}{\sqrt{a_\tau}} \epsilon_{\text{app}}(t). \quad (61)$$

Taking expectation with respect to $\boldsymbol{\lambda}_t$ and unrolling (61) for T steps results in

$$\mathbb{E}[W_2(p_T, \mu^*)] \leq \Psi_{0,T} W_2(p_0, q_T^{\boldsymbol{\lambda}^*}) + \sum_{t=0}^{T-1} \Psi_{t,T} \frac{b_{T-t}}{\sqrt{a_{T-t}}} \left(\gamma_t \mathbb{E}[\|\boldsymbol{\lambda}_t - \boldsymbol{\lambda}^*\|] + \epsilon_{\text{app}}(t) \right), \quad (62)$$

where $\Psi_{s,T} = \prod_{t=s+1}^T \rho_t$. For large T , it holds that $q_T^{\boldsymbol{\lambda}^*}$ converges to $\mathcal{N}(\mathbf{0}, \mathbf{I})$, making the first term go to zero. This completes the proof. \square

C.4 Gradient Bias

C.4.1 Tweedie's Error

Lemma 3. Consider the reverse diffusion sampler, defined in (7), associated with a dual value $\boldsymbol{\lambda}_t$. Then, under Assumptions 2, it holds that

$$\mathbb{E}_{\boldsymbol{\lambda}_t} \left[\left\| \mathbb{E}_{\tilde{p}_{t+1}} \left[\mathbf{f} \left(\mathbb{E}_{\tilde{\pi}_{t+1}} \left[\mathbf{y}_0 | \tilde{\mathbf{x}}_{t+1}, \boldsymbol{\lambda}_t \right] \right) \right] - \mathbb{E}_{\mu_{\boldsymbol{\lambda}_t}^\dagger} \left[\mathbf{f}(\mathbf{y}_0) \right] \right\|_2 \right] \leq L_f \epsilon_{TW}(t+1) \quad (63)$$

where \tilde{p}_t is the marginal distribution of the reverse process under fixed $\boldsymbol{\lambda}_t$, $\tilde{\pi}_t$ is the posterior density under the same process, L_f is a Lipschitz constant and ϵ_{TW} is the expected Tweedie posterior-mean error.

Proof. Define the joint distribution $\Pi_{t+1}^{\boldsymbol{\lambda}_t}(\mathbf{y}_0, \tilde{\mathbf{x}}_{t+1} | \boldsymbol{\lambda}_t) = \tilde{\pi}_{t+1}(\mathbf{y}_0 | \tilde{\mathbf{x}}_{t+1}, \boldsymbol{\lambda}_t) \tilde{p}_{t+1}(\tilde{\mathbf{x}}_{t+1} | \boldsymbol{\lambda}_t)$ with marginals $\mu_{\boldsymbol{\lambda}_t}^\dagger$ and \tilde{p}_{t+1} . Then, we can write the bias as

$$B_1(\boldsymbol{\lambda}_t) := \mathbb{E}_{\tilde{p}_{t+1}} \left[\mathbf{f} \left(\mathbb{E}_{\tilde{\pi}_{t+1}} \left[\mathbf{y}_0 | \tilde{\mathbf{x}}_{t+1}, \boldsymbol{\lambda}_t \right] \right) \right] - \mathbb{E}_{\mu_{\boldsymbol{\lambda}_t}^\dagger} \left[\mathbf{f}(\mathbf{y}_0) \right] \quad (64)$$

$$= \mathbb{E}_{\Pi_{t+1}^{\boldsymbol{\lambda}_t}} \left[\mathbf{f} \left(\mathbb{E}_{\tilde{\pi}_{t+1}} \left[\mathbf{y}_0 | \tilde{\mathbf{x}}_{t+1}, \boldsymbol{\lambda}_t \right] \right) - \mathbf{f}(\mathbf{y}_0) \mid \boldsymbol{\lambda}_t \right]. \quad (65)$$

Taking the norm and applying Jensen's inequality and Assumption 2, we get

$$\|B_1(\boldsymbol{\lambda}_t)\|_2^2 \leq \mathbb{E}_{\Pi_{t+1}^{\boldsymbol{\lambda}_t}} \left[\left\| \mathbf{f} \left(\mathbb{E}_{\tilde{\pi}_{t+1}} [\mathbf{y}_0 | \tilde{\mathbf{x}}_{t+1}, \boldsymbol{\lambda}_t] \right) - \mathbf{f}(\mathbf{y}_0) \right\|_2^2 \mid \boldsymbol{\lambda}_t \right] \quad (66)$$

$$\leq L_f^2 \mathbb{E}_{\Pi_{t+1}^{\boldsymbol{\lambda}_t}} \left[\left\| \mathbb{E}_{\tilde{\pi}_{t+1}} [\mathbf{y}_0 | \tilde{\mathbf{x}}_{t+1}, \boldsymbol{\lambda}_t] - \mathbf{y}_0 \right\|_2^2 \mid \boldsymbol{\lambda}_t \right]. \quad (67)$$

Take expectation with respect to $\boldsymbol{\lambda}_t$, then we have

$$\begin{aligned} \mathbb{E} \left[\|B_1(\boldsymbol{\lambda}_t)\|_2^2 \right] &\leq L_f^2 \mathbb{E}_{\boldsymbol{\lambda}_t} \mathbb{E}_{\Pi_{t+1}^{\boldsymbol{\lambda}_t}} \left\| \mathbb{E}_{\tilde{\pi}_{t+1}} [\mathbf{y}_0 | \tilde{\mathbf{x}}_{t+1}, \boldsymbol{\lambda}_t] - \mathbf{y}_0 \right\|_2^2 \\ &=: L_f^2 \epsilon_{TW}^2(t+1). \end{aligned} \quad (68)$$

where $\epsilon_{TW}^2(t+1)$ is the expected Tweedie posterior-mean error at step $t+1$. \square

C.4.2 Marginal Mismatch

Lemma 4. *Under Assumptions 4 and 5, it holds that*

$$\begin{aligned} &\left\| \mathbb{E}_{\tilde{p}_{t+1}} \left[\mathbf{f} \left(\mathbb{E}_{\tilde{\pi}_{t+1}} [\mathbf{y}_0 | \tilde{\mathbf{x}}_{t+1}, \boldsymbol{\lambda}_t] \right) \right] - \mathbb{E}_{p_{t+1}} \left[\mathbf{f} \left(\mathbb{E}_{\tilde{\pi}_{t+1}} [\mathbf{y}_0 | \mathbf{x}_{t+1}, \boldsymbol{\lambda}_t] \right) \right] \right\|_2 \\ &\leq L_h \sum_{j=0}^{t-1} \Psi_{j-1,t} \frac{b_{T-j}}{\sqrt{a_{T-j}}} \left(\gamma_j \|\boldsymbol{\lambda}_j - \boldsymbol{\lambda}_t\|_2 + \epsilon_j \right). \end{aligned} \quad (69)$$

where $\Psi_{s,t} = \prod_{r=s+1}^t \rho_r(\boldsymbol{\lambda}_r)$ is the stability product and ρ_r, γ_j are the moduli of Lemma 6 and Lemma 7, generalized to any given $\boldsymbol{\lambda}$.

Proof. We use synchronous coupling to compare the Tweedie posterior mean at step $t+1$ under two processes: 1) PDI, and 2) the reverse process (7) under $\boldsymbol{\lambda}_t$.

Under the PDI dynamics, one reverse step is given by

$$\mathbf{x}_{s+1} = \frac{1}{\sqrt{a_{T-s}}} \left(\mathbf{x}_s + b_{T-s} \mathbf{s}_\theta(\mathbf{x}_s, s, \boldsymbol{\lambda}_s) \right) + \sqrt{b_{T-s}} \boldsymbol{\epsilon}_s, \quad (70)$$

where $\mathbf{x}_s \sim p_s$ while the corresponding kernel $K_s^{\boldsymbol{\lambda}_t}$ under (7) with fixed $\boldsymbol{\lambda}_t$ is

$$\tilde{\mathbf{x}}_{s+1} = \frac{1}{\sqrt{a_{T-s}}} \left(\tilde{\mathbf{x}}_s + b_{T-s} \mathbf{s}_s(\tilde{\mathbf{x}}_s | \boldsymbol{\lambda}_t) \right) + \sqrt{b_{T-s}} \boldsymbol{\epsilon}_s. \quad (71)$$

Under the synchronous coupling, the two processes share the same noise $\boldsymbol{\epsilon}_s$ and the same initialization, i.e., $\mathbf{x}_0 = \tilde{\mathbf{x}}_0$. Thus, the difference between the two noisy samples \mathbf{x}_{s+1} and $\tilde{\mathbf{x}}_{s+1}$ is

$$\begin{aligned} \mathbf{x}_{s+1} - \tilde{\mathbf{x}}_{s+1} &= \frac{1}{\sqrt{a_{T-s}}} \left(\mathbf{x}_s - \tilde{\mathbf{x}}_s \right) + \frac{b_{T-s}}{\sqrt{a_{T-s}}} \left(\mathbf{s}_s(\mathbf{x}_s | \boldsymbol{\lambda}_s) - \mathbf{s}_s(\tilde{\mathbf{x}}_s | \boldsymbol{\lambda}_s) \right) \\ &\quad + \frac{b_{T-s}}{\sqrt{a_{T-s}}} \left(\mathbf{s}_\theta(\mathbf{x}_s, s, \boldsymbol{\lambda}_s) - \mathbf{s}_s(\mathbf{x}_s | \boldsymbol{\lambda}_s) \right) \\ &\quad + \frac{b_{T-s}}{\sqrt{a_{T-s}}} \left(\mathbf{s}_s(\tilde{\mathbf{x}}_s | \boldsymbol{\lambda}_s) - \mathbf{s}_s(\tilde{\mathbf{x}}_s | \boldsymbol{\lambda}_t) \right), \end{aligned} \quad (72)$$

where we added and subtracted $\frac{b_{T-s}}{\sqrt{a_{T-s}}} (\mathbf{s}_s(\tilde{\mathbf{x}}_s | \boldsymbol{\lambda}_s) + \mathbf{s}_s(\mathbf{x}_s | \boldsymbol{\lambda}_s))$. These quantities have been analyzed in Lemmas 6 and 7 for the optimal kernel $K_t^{\boldsymbol{\lambda}^*}$. Here, we use generalized formulas for any kernel associated with (7). Similarly to (97)–(101), we can bound the first term with

$$\left\| \frac{1}{\sqrt{a_{T-s}}} \left(\mathbf{x}_s - \tilde{\mathbf{x}}_s \right) + \frac{b_{T-s}}{\sqrt{a_{T-s}}} \left(\mathbf{s}_s(\mathbf{x}_s | \boldsymbol{\lambda}_s) - \mathbf{s}_s(\tilde{\mathbf{x}}_s | \boldsymbol{\lambda}_s) \right) \right\|_2 \leq \rho_s(\boldsymbol{\lambda}_s) \cdot \|\mathbf{x}_s - \tilde{\mathbf{x}}_s\|_2, \quad (73)$$

where $\rho_s(\boldsymbol{\lambda}_s) = \frac{1}{\sqrt{a_{T-s}}} \sup_{\mathbf{x}} \left\| \mathbf{I} + b_{T-s} \nabla_{\mathbf{x}}^2 \log q_{T-s}(\mathbf{x} | \boldsymbol{\lambda}_s) \right\|_{\text{op}}$ is the stability factor of the one-step kernel $K_s^{\boldsymbol{\lambda}_s}$. For the last term, we follow (103)–(107) to get

$$\|\mathbf{s}_s(\tilde{\mathbf{x}}_s | \boldsymbol{\lambda}_s) - \mathbf{s}_s(\tilde{\mathbf{x}}_s | \boldsymbol{\lambda}_t)\|_2 \leq \gamma_s \cdot \|\boldsymbol{\lambda}_s - \boldsymbol{\lambda}_t\|_2, \quad (74)$$

where $\gamma_s = \frac{R\alpha_{T-s}}{\beta\sigma_{T-s}^2} \sqrt{\sup_{\boldsymbol{\lambda} \in \Lambda} \|\mathbf{Cov}_{\pi_s}(\mathbf{y}_0 | \tilde{\mathbf{x}}_s, \boldsymbol{\lambda})\|_{\text{op}}}$.

Combining the two results, along with Assumption 4, we obtain

$$\begin{aligned} \|\mathbf{x}_{s+1} - \tilde{\mathbf{x}}_{s+1}\|_2 &\leq \rho_s(\boldsymbol{\lambda}_s) \cdot \|\mathbf{x}_s - \tilde{\mathbf{x}}_s\|_2 \\ &\quad + \frac{b_{T-s}}{\sqrt{a_{T-s}}} \left(\gamma_s \|\boldsymbol{\lambda}_s - \boldsymbol{\lambda}_t\|_2 + \|\mathbf{s}_\theta(\mathbf{x}_s, s, \boldsymbol{\lambda}_s) - \mathbf{s}_s(\mathbf{x}_s | \boldsymbol{\lambda}_s)\|_2 \right). \end{aligned} \quad (75)$$

Then, we take expectation with respect to the coupling Π_{s+1} to get

$$\begin{aligned} \mathbb{E}_{\Pi_{s+1}} \left[\|\mathbf{x}_{s+1} - \tilde{\mathbf{x}}_{s+1}\|_2 \right] &\leq \rho_s(\boldsymbol{\lambda}_s) \cdot \mathbb{E}_{\Pi_s} \left[\|\mathbf{x}_s - \tilde{\mathbf{x}}_s\|_2 \right] \\ &\quad + \frac{b_{T-s}}{\sqrt{a_{T-s}}} \left(\gamma_s \cdot \|\boldsymbol{\lambda}_s - \boldsymbol{\lambda}_t\|_2 + \mathbb{E}_{p_s} \|\mathbf{s}_\theta(\mathbf{x}_s, s, \boldsymbol{\lambda}_s) - \mathbf{s}_s(\mathbf{x}_s | \boldsymbol{\lambda}_s)\|_2 \right) \\ &\leq \rho_s(\boldsymbol{\lambda}_s) \cdot \mathbb{E}_{\Pi_s} \left[\|\mathbf{x}_s - \tilde{\mathbf{x}}_s\|_2 \right] + \frac{b_{T-s}}{\sqrt{a_{T-s}}} \left(\gamma_s \cdot \|\boldsymbol{\lambda}_s - \boldsymbol{\lambda}_t\|_2 + \epsilon_s \right). \end{aligned} \quad (76)$$

The last inequality follows from Assumption 4 and Jensen's inequality. With this inequality in place, let $\mathbf{h}(\mathbf{x}_t) := \mathbf{f} \left(\mathbb{E}_{\tilde{\pi}_{t+1}} [\mathbf{y}_0 | \mathbf{x}_{t+1}, \boldsymbol{\lambda}_t] \right)$, and bound the bias with

$$\begin{aligned} \|B_2(\boldsymbol{\lambda}_t; \mathcal{F}_t)\|_2 &:= \left\| \mathbb{E}_{\tilde{p}_t} [\mathbf{h}(\tilde{\mathbf{x}}_{t+1})] - \mathbb{E}_{p_t} [\mathbf{h}(\mathbf{x}_{t+1})] \right\|_2 \\ &= \left\| \mathbb{E}_{\Pi_t} [\mathbf{h}(\tilde{\mathbf{x}}_{t+1}) - \mathbf{h}(\mathbf{x}_{t+1})] \right\|_2 \end{aligned} \quad (77)$$

$$\leq L_h \mathbb{E}_{\Pi_{t+1}} \|\tilde{\mathbf{x}}_{t+1} - \mathbf{x}_{t+1}\|_2 \quad (78)$$

$$\leq L_h \left(\rho_t(\boldsymbol{\lambda}_t) \cdot \mathbb{E}_{\Pi_t} [\|\mathbf{x}_t - \tilde{\mathbf{x}}_t\|_2] + \frac{b_{T-t}}{\sqrt{a_{T-t}}} (\gamma_t \cdot \|\boldsymbol{\lambda}_t - \boldsymbol{\lambda}_t\|_2 + \epsilon_{\text{app}}(t)) \right), \quad (79)$$

where L_h is the Lipschitz constant of $\mathbf{h}(\mathbb{E}_{\tilde{\pi}_{t+1}} [\mathbf{y}_0 | \mathbf{x}_{t+1}, \boldsymbol{\lambda}_t])$ and depends on L_f and the score function. The dual mismatch here is zero but we keep it to show the decomposition of one recursion step.

Recursively, we get the bound:

$$\|B_2(\boldsymbol{\lambda}_t; \mathcal{F}_t)\|_2 \leq L_h \sum_{j=0}^t \left(\prod_{s=j}^t \rho_s(\boldsymbol{\lambda}_s) \right) \cdot \frac{b_{T-j}}{\sqrt{a_{T-j}}} \left(\gamma_j \|\boldsymbol{\lambda}_j - \boldsymbol{\lambda}_t\|_2 + \epsilon_{\text{app}}(j) \right) \quad (80)$$

Let $\Psi_{j-1,t} = \prod_{s=j}^t \rho_s(\boldsymbol{\lambda}_s)$ be the product of the stability coefficient over the past $t-j$ steps, then

$$\|B_2(\boldsymbol{\lambda}_t; \mathcal{F}_t)\|_2 \leq L_h \sum_{j=0}^t \Psi_{j-1,t} \frac{b_{T-j}}{\sqrt{a_{T-j}}} \left(\gamma_j \|\boldsymbol{\lambda}_j - \boldsymbol{\lambda}_t\|_2 + \epsilon_{\text{app}}(j) \right). \quad (81)$$

It is worth noting that

$$\frac{b_{T-j}}{\sqrt{a_{T-j}}} \gamma_j = \frac{b_{T-j}}{\sqrt{a_{T-j}}} \frac{\alpha_{T-j}}{\sigma_{T-j}^2} \frac{R}{\beta} \sqrt{\sup_{\boldsymbol{\lambda} \in \Lambda} \|\mathbf{Cov}_{\pi_s}(\mathbf{y}_0 | \tilde{\mathbf{x}}_j, \boldsymbol{\lambda})\|_{\text{op}}}$$

where $\frac{b_{T-j}}{\sqrt{a_{T-j}}} \frac{\alpha_{T-j}}{\sigma_{T-j}^2} = \alpha_{T-j-1} b_{T-j} / (b_{T-j} + a_{T-j} \sigma_{T-j-1}^2)$ is a non-negative value under 1 for variance-preserving noise schedules. Therefore, the bias depends on the noise schedule mainly through the stability product $\Psi_{j-1,t}$.

Now assume that, for all $t \leq T$, it holds that

$$\sum_{j=0}^t \Psi_{j-1,t} \frac{b_{T-j}}{\sqrt{a_{T-j}}} \gamma_j (t-j) \leq C_{\text{hist}} < \infty, \quad (82)$$

and

$$\sum_{j=0}^t \Psi_{j-1,t} \frac{b_{T-j}}{\sqrt{a_{T-j}}} \epsilon_{\text{app}}(j) \leq \epsilon_{\text{hist}} < \infty. \quad (83)$$

It is also true that

$$\|\boldsymbol{\lambda}_j - \boldsymbol{\lambda}_t\|_2 \leq (t - j)\eta R. \quad (84)$$

Therefore, we have $\|B_2(\boldsymbol{\lambda}_t; \mathcal{F}_t)\|_2^2 \leq (1 + \delta)L_h^2 C_{\text{hist}}^2 \eta^2 R^2 + (1 + \frac{1}{\delta})L_h^2 \epsilon_{\text{hist}}^2$, for an arbitrary $\delta > 0$, using Young's inequality, which completes the proof. \square

As discussed in Section 4, under noise schedules with a sufficiently long stable high-noise phase, the stability products decay with the length of the history window. Hence, contributions from early dual mismatches are damped, and only the recent history can have a non-negligible effect near the high-SNR region, where the reverse dynamics become more sensitive. In this regime, the remaining history-dependent contribution can be controlled by the step size η_t .

C.4.3 Parameterization Error

Lemma 5. *Under Assumptions 2 and 4, it holds that*

$$\left\| \mathbb{E}_{p_{t+1}} \left[\mathbf{f} \left(\mathbb{E}_{\tilde{\pi}_{t+1}^\theta} [\mathbf{y}_0 | \mathbf{x}_{t+1}, \boldsymbol{\lambda}_t] \right) - \mathbf{f} \left(\mathbb{E}_{\tilde{\pi}_{t+1}} [\mathbf{y}_0 | \mathbf{x}_{t+1}, \boldsymbol{\lambda}_t] \right) \right] \right\|_2^2 \leq L_f^2 \frac{\sigma_{T-t}^4}{\bar{\alpha}_{T-t}^2} \epsilon_{\text{app}}^2 (t+1). \quad (85)$$

Proof. The Tweedie posterior means are given as

$$\mathbb{E}_{\tilde{\pi}_{t+1}^\theta} [\mathbf{y}_0 | \mathbf{x}_{t+1}, \boldsymbol{\lambda}_t] = \frac{1}{\bar{\alpha}_{T-t}} \left(\mathbf{x}_{t+1} + \sigma_{T-t}^2 \mathbf{s}_\theta(\mathbf{x}_{t+1}, t+1, \boldsymbol{\lambda}_t) \right), \quad (86)$$

$$\mathbb{E}_{\tilde{\pi}_{t+1}} [\mathbf{y}_0 | \mathbf{x}_{t+1}, \boldsymbol{\lambda}_t] = \frac{1}{\bar{\alpha}_{T-t}} \left(\mathbf{x}_{t+1} + \sigma_{T-t}^2 \mathbf{s}_{t+1}(\mathbf{x}_{t+1} | \boldsymbol{\lambda}_t) \right), \quad (87)$$

where $\bar{\alpha}_{T-t} = \max\{\alpha_{\min}, \alpha_{T-t}\}$. Therefore, we have

$$\left\| \mathbb{E}_{p_{t+1}} \left[\mathbf{f} \left(\mathbb{E}_{\tilde{\pi}_{t+1}^\theta} [\mathbf{y}_0 | \mathbf{x}_{t+1}, \boldsymbol{\lambda}_t] \right) - \mathbf{f} \left(\mathbb{E}_{\tilde{\pi}_{t+1}} [\mathbf{y}_0 | \mathbf{x}_{t+1}, \boldsymbol{\lambda}_t] \right) \right] \right\|_2 \quad (88)$$

$$\leq L_f \frac{\sigma_{T-t}^2}{\bar{\alpha}_{T-t}} \mathbb{E}_{p_{t+1}} \left\| \mathbf{s}_\theta(\mathbf{x}_{t+1}, t+1, \boldsymbol{\lambda}_t) - \mathbf{s}_{t+1}(\mathbf{x}_{t+1} | \boldsymbol{\lambda}_t) \right\|_2 \leq L_f \frac{\sigma_{T-t}^2}{\bar{\alpha}_{T-t}} \epsilon_{t+1}, \quad (89)$$

by Jensen's inequality and Assumptions 2 and 4. \square

C.5 Proof of Proposition 2

Proof. Let π be any coupling between ν and μ . Apply the synchronous coupling (same noise ϵ_t) to each realized pair $(\mathbf{x}, \mathbf{y}) \sim \pi$:

$$\mathbf{X}^+ = \frac{1}{\sqrt{a_{T-t}}} \left(\mathbf{x} + b_{T-t} \nabla \log q_{T-t}(\mathbf{x} | \boldsymbol{\lambda}^*) \right) + \sqrt{b_{T-t}} \boldsymbol{\epsilon}_t \quad (90)$$

$$\mathbf{Y}^+ = \frac{1}{\sqrt{a_{T-t}}} \left(\mathbf{y} + b_{T-t} \nabla \log q_{T-t}(\mathbf{y} | \boldsymbol{\lambda}^*) \right) + \sqrt{b_{T-t}} \boldsymbol{\epsilon}_t \quad (91)$$

Let Γ be the joint law of $(\mathbf{X}^+, \mathbf{Y}^+)$. By construction, the marginal distribution of \mathbf{X}^+ is $\nu K_t^{\boldsymbol{\lambda}^*}$, and the marginal distribution of \mathbf{Y}^+ is $\mu K_t^{\boldsymbol{\lambda}^*}$. Therefore, Γ is a valid coupling between $\nu K_t^{\boldsymbol{\lambda}^*}$ and $\mu K_t^{\boldsymbol{\lambda}^*}$.

Using the definition of W_2 , we have

$$W_2^2(\nu K_t^{\boldsymbol{\lambda}^*}, \mu K_t^{\boldsymbol{\lambda}^*}) \leq \mathbb{E}_\Gamma [\|\mathbf{X}^+ - \mathbf{Y}^+\|^2] \quad (92)$$

$$= \mathbb{E}_{(\mathbf{x}, \mathbf{y}) \sim \pi} \left[\mathbb{E} [\|\mathbf{X}^+ - \mathbf{Y}^+\|^2 | \mathbf{x}, \mathbf{y}] \right] \quad (93)$$

$$\leq \rho_t^2 \mathbb{E}_{(\mathbf{x}, \mathbf{y}) \sim \pi} [\|\mathbf{x} - \mathbf{y}\|^2], \quad (94)$$

which follows by Lemma 6. Note that, conditioned on the pair (\mathbf{x}, \mathbf{y}) , $\|\mathbf{X}^+ - \mathbf{Y}^+\|^2$ is deterministic and the inner expectation in (93) is trivial. Since this holds for every coupling $\pi \in \Pi(\nu, \mu)$, we take the infimum over π and obtain

$$W_2^2(\nu K_t^{\boldsymbol{\lambda}^*}, \mu K_t^{\boldsymbol{\lambda}^*}) \leq \rho_t^2 W_2^2(\nu, \mu). \quad (95)$$

Taking square roots gives

$$W_2(\nu K_t^{\boldsymbol{\lambda}^*}, \mu K_t^{\boldsymbol{\lambda}^*}) \leq \rho_t W_2(\nu, \mu). \quad (96)$$

This proves the proposition. \square

C.6 Additional Lemmas

Lemma 6 (One-step contraction modulus). *Under Assumption 5, for any \mathbf{x}, \mathbf{y} and under the synchronous coupling (common noise ϵ_t), the reverse-step outputs satisfy $\|\mathbf{X}^+ - \mathbf{Y}^+\|^2 \leq \rho_t^2 \|\mathbf{x} - \mathbf{y}\|^2$, almost surely, with*

$$\rho_t = \frac{1}{\sqrt{a_{T-t}}} \sup_{\mathbf{x}} \left\| \mathbf{I} + b_{T-t} \nabla_{\mathbf{x}}^2 \log q_{T-t}(\mathbf{x} | \boldsymbol{\lambda}^*) \right\|_{\text{op}}.$$

Proof. Under synchronous coupling, we have

$$\mathbf{X}^+ - \mathbf{Y}^+ = \frac{1}{\sqrt{a_{T-t}}} \left(\mathbf{x} - \mathbf{y} + b_{T-t} (\nabla \log q_{T-t}(\mathbf{x} | \boldsymbol{\lambda}^*) - \nabla \log q_{T-t}(\mathbf{y} | \boldsymbol{\lambda}^*)) \right). \quad (97)$$

The noise cancels exactly since the two processes share the same noise. Thus, this is deterministic given \mathbf{x} and \mathbf{y} . Then by the mean value theorem along the segment from \mathbf{y} to \mathbf{x} , we get

$$\nabla \log q_{T-t}(\mathbf{x} | \boldsymbol{\lambda}^*) - \nabla \log q_{T-t}(\mathbf{y} | \boldsymbol{\lambda}^*) = \left(\int_0^1 \nabla^2 \log q_{T-t}(\mathbf{y} + s(\mathbf{x} - \mathbf{y}) | \boldsymbol{\lambda}^*) ds \right) \cdot (\mathbf{x} - \mathbf{y}). \quad (98)$$

Substitute back into (97), we get

$$\mathbf{X}^+ - \mathbf{Y}^+ = \frac{1}{\sqrt{a_{T-t}}} (\mathbf{I} + b_{T-t} \widehat{\mathbf{H}}) \cdot (\mathbf{x} - \mathbf{y}), \quad (99)$$

where $\widehat{\mathbf{H}}$ is the averaged Hessian along the segment. Taking norms,

$$\|\mathbf{X}^+ - \mathbf{Y}^+\| \leq \frac{1}{\sqrt{a_{T-t}}} \left\| \mathbf{I} + b_{T-t} \widehat{\mathbf{H}} \right\|_{\text{op}} \cdot \|\mathbf{x} - \mathbf{y}\| \quad (100)$$

$$\leq \frac{1}{\sqrt{a_{T-t}}} \sup_{\mathbf{x} \in \mathcal{X}} \left\| \mathbf{I} + b_{T-t} \nabla_{\mathbf{x}}^2 \log q_{T-t}(\mathbf{x} | \boldsymbol{\lambda}^*) \right\|_{\text{op}} \|\mathbf{x} - \mathbf{y}\| =: \rho_t \|\mathbf{x} - \mathbf{y}\|. \quad (101)$$

The last inequality upper bounded the averaged Hessian with the supremum over the compact domain \mathcal{X} . This completes the proof. \square

Lemma 7. *Under Assumption 2, the score function $\mathbf{s}_t(\cdot | \boldsymbol{\lambda})$ is Lipschitz in $\boldsymbol{\lambda}$, and*

$$\|\mathbf{s}_t(\mathbf{x} | \boldsymbol{\lambda}_t) - \mathbf{s}_t(\mathbf{x} | \boldsymbol{\lambda}^*)\| \leq \gamma_t \|\boldsymbol{\lambda}_t - \boldsymbol{\lambda}^*\|_2, \quad (102)$$

and $\gamma_t = \frac{R\alpha_{T-t}}{\beta\sigma_{T-t}^2} \sqrt{\sup_{\boldsymbol{\lambda}} \|\mathbf{Cov}_{\pi_t}(\mathbf{y}_0 | \mathbf{x}, \boldsymbol{\lambda})\|_{\text{op}}} \geq 0$.

Proof. Using the mean value theorem, we can then bound the difference by

$$\|\mathbf{s}_t(\mathbf{x} | \boldsymbol{\lambda}_t) - \mathbf{s}_t(\mathbf{x} | \boldsymbol{\lambda}^*)\| \leq \left(\sup_{\boldsymbol{\lambda}} \|\nabla_{\boldsymbol{\lambda}} \mathbf{s}_t(\mathbf{x} | \boldsymbol{\lambda})\|_{\text{op}} \right) \|\boldsymbol{\lambda}_t - \boldsymbol{\lambda}^*\|_2, \quad (103)$$

where $\|\cdot\|_{\text{op}}$ is the operator norm. The score function is defined through the Tweedie as

$$\mathbf{s}_t(\mathbf{x} | \boldsymbol{\lambda}) = \frac{1}{\sigma_{T-t}^2} \left(\alpha_{T-t} \mathbb{E}_{\pi_t}[\mathbf{y}_0 | \mathbf{x}, \boldsymbol{\lambda}] - \mathbf{x} \right), \quad (104)$$

where π_t is the posterior distribution:

$$\pi_t(\mathbf{y}_0 | \mathbf{x}, \boldsymbol{\lambda}) \propto \frac{1}{Z(\boldsymbol{\lambda})} \exp \left(-E(\mathbf{y}_0, \boldsymbol{\lambda}_t) - \frac{1}{2\sigma_{T-t}^2} \|\mathbf{x} - \alpha_{T-t} \mathbf{y}_0\|^2 \right). \quad (105)$$

The posterior depends on $\boldsymbol{\lambda}$ only through the prior. Thus, we have

$$\nabla_{\boldsymbol{\lambda}} \mathbb{E}_{\pi_t}[\mathbf{y}_0 | \mathbf{x}, \boldsymbol{\lambda}] = \frac{-1}{\beta} \mathbf{Cov}_{\pi_t}(\mathbf{y}_0, \mathbf{f}(\mathbf{y}_0) | \mathbf{x}, \boldsymbol{\lambda}). \quad (106)$$

Taking the operator norm, we get

$$\frac{\beta\sigma_{T-t}^2}{\alpha_{T-t}} \|\nabla_{\boldsymbol{\lambda}} \mathbf{s}_t(\mathbf{x} | \boldsymbol{\lambda})\|_{\text{op}} \leq \left(\|\mathbf{Cov}_{\pi_t}(\mathbf{y}_0 | \mathbf{x}, \boldsymbol{\lambda})\|_{\text{op}} \right)^{1/2} \cdot \left(\|\mathbf{Cov}_{\pi_t}(\mathbf{f}(\mathbf{y}_0) | \mathbf{x}, \boldsymbol{\lambda})\|_{\text{op}} \right)^{1/2} \quad (107)$$

$$\leq R \sqrt{\|\mathbf{Cov}_{\pi_t}(\mathbf{y}_0 | \mathbf{x}, \boldsymbol{\lambda})\|_{\text{op}}}, \quad (108)$$

using Assumption 2. Let $\gamma_t = \frac{R\alpha_{T-t}}{\beta\sigma_{T-t}^2} \sqrt{\sup_{\boldsymbol{\lambda}} \|\mathbf{Cov}_{\pi_t}(\mathbf{y}_0 | \mathbf{x}, \boldsymbol{\lambda})\|_{\text{op}}}$ to complete the proof. \square

Lemma 8. *The Lagrangian function in (2) is also equivalent to*

$$\mathcal{L}(\mu, \boldsymbol{\lambda}) = \beta D_{\text{KL}}(\mu \| \mu_{\boldsymbol{\lambda}}^\dagger) + g(\boldsymbol{\lambda}).$$

Proof. Start with the definition of KL divergence:

$$D_{\text{KL}}(\mu \| \mu_{\boldsymbol{\lambda}_t}^\dagger) = \mathbb{E}_\mu \left[\log \mu(\mathbf{x}) - \log \mu_{\boldsymbol{\lambda}_t}^\dagger(\mathbf{x}) \right] \quad (109)$$

$$= \mathbb{E}_\mu [\log \mu(\mathbf{x})] + \frac{1}{\beta} \mathbb{E}_\mu \left[f_0(\mathbf{x}) + \boldsymbol{\lambda}^\top \mathbf{f}(\mathbf{x}) \right] + \log Z(\boldsymbol{\lambda}) \quad (110)$$

$$= \frac{1}{\beta} \mathcal{L}(\mu, \boldsymbol{\lambda}) + \log Z(\boldsymbol{\lambda}). \quad (111)$$

The second equality follows from the definition of $\mu_{\boldsymbol{\lambda}_t}^\dagger$ while the last one uses the definition of the Lagrangian. With the fact that $g(\boldsymbol{\lambda}) = -\beta \log Z(\boldsymbol{\lambda})$, we complete the proof. \square

D Discussions

D.1 Dual Training

PDI updates the dual variables during inference, allowing the sampler to react instantaneously to constraint violations. Another alternative is to estimate the optimal dual variables during training while training a score model to sample directly from the optimal distribution. We refer to this approach as dual training (DT). The idea behind DT is related to prior work on constrained diffusion models [15, 16]. However, this prior work typically considers a single optimization problem, such as fine-tuning a pre-trained model to satisfy a fixed set of constraints, where there is only one optimal dual variable to estimate. In contrast, our formulation considers a family of problem instances, each with its own optimal distribution and corresponding optimal dual variable. In this section, we extend DT to this setting by estimating the dual variables separately for each problem instance during training. The resulting method then serves as an ablation baseline to test the effect of inference-time dual updates.

The dual problem in (3), for a given problem instance \mathcal{G} , can be re-written as a bi-level problem,

$$D^*(\mathcal{G}) = \max_{\boldsymbol{\lambda} \succeq \mathbf{0}} \mathcal{L}(\mu_{\boldsymbol{\lambda}}^\dagger, \boldsymbol{\lambda}; \mathcal{G})$$

$$\text{with } \mu_{\boldsymbol{\lambda}}^\dagger = \operatorname{argmin}_{\mu \in \mathcal{P}_2} \mathcal{L}(\mu, \boldsymbol{\lambda}; \mathcal{G}). \quad (112)$$

The inner problem is equivalent to an unconstrained sampling problem and the diffusion process defined in (6)–(7) provides a mechanism to sample from the target distribution $\mu_{\boldsymbol{\lambda}}^\dagger$. Therefore, we replace the inner problem with the problem of training the score model of the reverse process (7). Let $\mathbf{s}_\phi(\mathbf{x}, t, \mathcal{G})$ be the score model, parameterized by ϕ , and p_T^ϕ be the terminal distribution of the reverse process under a given dual variable $\boldsymbol{\lambda}$. The parameterized bi-level problem can then be cast as

$$D_\phi^*(\mathcal{G}) = \max_{\boldsymbol{\lambda} \succeq \mathbf{0}} \mathcal{L}(p_T^{\phi, \boldsymbol{\lambda}}, \boldsymbol{\lambda}; \mathcal{G})$$

$$\text{with } \phi_{\boldsymbol{\lambda}}(\mathcal{G}) = \operatorname{argmin}_{\phi} \mathbb{E}_{t, \mathbf{x}_t} \left[\omega(t) \left\| \mathbf{s}_\phi(\mathbf{x}_t, t, \mathcal{G}) - \nabla \log q_{T-t}(\mathbf{x}_t | \boldsymbol{\lambda}; \mathcal{G}) \right\|_2^2 \right], \forall \boldsymbol{\lambda}. \quad (113)$$

The expectation is with respect to the noisy samples and the diffusion time. The inner problem in its current form assigns a different parametrization ϕ for each dual variable $\boldsymbol{\lambda}$ and problem instance \mathcal{G} . This is not a training objective and is generally infeasible. To overcome this challenge, we alternate between the two problems so that, for an outer iteration k , the score model is trained only against the most recent dual variable, which is then updated based on the recent constraint violations. More concretely, the training algorithm follows the following dual-ascent iterations:

$$\phi_k = \operatorname{argmin}_{\phi} \mathbb{E}_{\mathcal{G}, t, \mathbf{x}_t} \left[\omega(t) \left\| \mathbf{s}_\phi(\mathbf{x}_t, t, \mathcal{G}) - \nabla \log q_{T-t}(\mathbf{x}_t | \boldsymbol{\lambda}_k(\mathcal{G}); \mathcal{G}) \right\|_2^2 \right], \quad (114)$$

$$\boldsymbol{\lambda}_{k+1}(\mathcal{G}) = \left[\boldsymbol{\lambda}_k(\mathcal{G}) + \eta_{\text{DT}} \mathbb{E}_{p_T^{\phi_k}} [\mathbf{f}(\mathbf{x}_T; \mathcal{G})] \right]_+, \forall \mathcal{G}, \quad (115)$$

Algorithm 3 Dual Training

```
1: Initialize  $\lambda(\mathcal{G}) \leftarrow \lambda_0$  for all  $\mathcal{G}$ 
2: Initialize score network  $\mathbf{s}_\phi$ 
3: for  $d = 1, \dots, D$  do ▷ Outer: dual iterations
4:   Initialize replay buffer  $\mathcal{B} \leftarrow \emptyset$ 
5:   for each problem  $\mathcal{G}$  in a batch  $\mathcal{B}_{\text{train}}$  do
6:     Rollout: sample  $\mathbf{x}_0^{(i)} \sim \mathcal{N}(\mathbf{0}, \mathbf{I})$ ; run inference with  $\mathbf{s}_\phi$  to obtain  $\{(\mathbf{x}_t^{(i)}, t)\}_{t=0}^{T-1}, \forall i \in [I]$ 
7:     Push  $\{(\mathbf{x}_t^{(i)}, t, \mathcal{G})\}_{i,t}$  to  $\mathcal{B}$ 
8:   end for
9:   for  $e = 1, \dots, E$  do ▷ Inner: train at fixed  $\lambda$ 
10:    Sample a minibatch  $\{(\mathbf{x}_t^{(j)}, t^{(j)}, \mathcal{G}^{(j)})\}_{j=1}^B$  from  $\mathcal{B}$ 
11:    for  $j = 1, \dots, B$  do
12:      if Bernoulli( $\rho_{\text{pert}}$ ) = 1 then ▷ Perturb the sample
13:         $\mathbf{x}_t^{(j)} \leftarrow \mathbf{x}_t^{(j)} + \epsilon_{\mathbf{x}} \cdot \mathbf{z}_x, \quad \mathbf{z}_x \sim \mathcal{N}(\mathbf{0}, \mathbf{I})$ 
14:      end if
15:    end for
16:     $\phi \leftarrow \phi - \alpha \nabla_{\frac{1}{B}} \sum_j w(t^{(j)}) \|\mathbf{s}_\phi(\mathbf{x}_t^{(j)}, t^{(j)}, \mathcal{G}^{(j)}) - \nabla \log q_{T-t^{(j)}}(\mathbf{x}_t^{(j)} \mid \lambda(\mathcal{G}^{(j)}); \mathcal{G}^{(j)})\|_2^2$ 
17:  end for
18:  for each problem  $\mathcal{G}$  in a batch  $\mathcal{B}_\lambda$  do ▷ Dual ascent
19:    Generate samples  $\{\mathbf{x}_T^{(i)} \sim p_T^\phi\}_{i=1}^I$  via full reverse diffusion using the most recent  $\phi$ 
20:     $\lambda(\mathcal{G}) \leftarrow \left[ \lambda(\mathcal{G}) + \eta_{\text{DT}} \sum_i \mathbf{f}(\mathbf{x}_T^{(i)}; \mathcal{G}) / I \right]_+$ 
21:  end for
22: end for
23: return  $\phi$ 
```

where η_{DT} is the dual step size. The expectation in the training objective becomes jointly over diffusion time, noisy samples, and the problem distribution so that a single \mathcal{G} -conditional parameterization learns the score field for a family of problems. The dual variables, however, remain instance-specific. Each problem instance \mathcal{G} maintains its own multiplier $\lambda_k(\mathcal{G})$, updated only from the constraint violations observed for that instance.

Updating the dual variables requires estimating the constraint violations under the current sampler, which in turn requires running the full reverse process to obtain clean samples. Implementing (114)–(115) to completion would therefore be computationally prohibitive. In practice, we use an alternating implementation. We perform a few gradient steps on the score-matching objective in (114), then update the dual variables for a subset of problem instances. Specifically, at each outer iteration, Algorithm 3 samples a batch of instances \mathcal{B}_λ and updates only their corresponding multipliers, while the remaining dual variables are kept unchanged. As in Algorithm 1, the score target is computed using the MC estimator in (16) and the noisy samples \mathbf{x}_t are obtained from rollouts of the inference dynamics at the beginning of each outer iteration.

At inference time, DT starts from Gaussian noise and runs the reverse diffusion process using the trained score model $\mathbf{s}_{\phi^*}(\mathbf{x}_t, t, \mathcal{G})$. For a test instance \mathcal{G} , the reverse dynamics are

$$\mathbf{x}_{t+1} = \frac{1}{\sqrt{a_{T-t}}} \left(\mathbf{x}_t + b_{T-t} \mathbf{s}_{\phi^*}(\mathbf{x}_t, t, \mathcal{G}) \right) + \sqrt{b_{T-t}} \epsilon_t. \quad (116)$$

No dual variable is initialized, provided to the score model, or updated during this process. The constraint information enters only through the learned parameters ϕ^* , which were trained using the instance-dependent dual estimates in (114)–(115). Thus, DT produces samples in a single reverse pass and does not adapt the trajectory to constraint violations observed during inference.

D.2 DT Challenges

Since we execute a few gradient steps instead of fully solving the minimization problem for each outer iteration, it is sensible to assume that the score model at iteration k satisfies

$$\phi_k \approx \underset{\phi}{\operatorname{argmin}} \mathbb{E}_{\mathcal{G}, t, \mathbf{x}_t} \mathbb{E}_{\lambda \sim \pi_k(\cdot | \mathcal{G})} \left[\omega(t) \left\| \mathbf{s}_\phi(\mathbf{x}_t, t, \mathcal{G}) - \nabla \log q_{T-t}(\mathbf{x}_t | \lambda; \mathcal{G}) \right\|_2^2 \right], \quad (117)$$

where $\pi_k(\cdot | \mathcal{G}) = \sum_{i=0}^k w_i \delta_{\lambda_i(\mathcal{G})}$ captures the mixture of dual variables encountered in the preceding training iterations and $\sum_i w_i = 1$. The weights w_i reflect the effective contribution of each past dual iterate to the score-model parameters. Although each dual iterate is used only once in (114), later iterates typically have stronger weights because their gradient updates are applied closer to the final parameter state. Since the dual variable is not provided as an input to the score model, the corresponding predictor is an averaged score field,

$$\mathbf{s}_{\phi_k}(\mathbf{x}_t, t, \mathcal{G}) \approx \mathbb{E}_{\lambda \sim \pi_k(\cdot | \mathcal{G})} \left[\nabla_{\mathbf{x}_t} \log q_{T-t}(\mathbf{x}_t | \lambda; \mathcal{G}) \right]. \quad (118)$$

This averaging is benign when the dual distribution collapses into a degenerate distribution of a single value close to the optimum or when the conditional scores associated with the dual iterates are nearly aligned.

However, for binding and near-binding constraints, where the constraint residual is close to zero, small changes in the generated samples change the constraint residual and therefore the multiplier update. As a result, the score model is trained on targets associated with a local range of dual values around the equilibrium. When two of these multipliers induce noticeably different score directions or correction strengths, the averaged score no longer matches the score associated with either dual value exactly. DT can therefore retain the part of the correction that is common across the dual trajectory, but it loses the multiplier-specific deviations. This explains why DT can still learn a reasonable constrained sampler when the dual trajectory repeatedly emphasizes the same constraints, while remaining less accurate for binding or near-binding constraints whose correction strength depends on the exact dual variable.

This limitation is amplified at test time for unseen problem instances. In DT, no multiplier is inferred during sampling. Therefore, for a new instance, the model must implicitly infer from the problem data which constraints are active and what correction strength is needed. When the new instance induces multipliers close to those encountered during training, DT can still perform well. However, if the new instance changes the binding constraints or requires noticeably different multiplier magnitudes, the learned averaged score field has no explicit mechanism to adapt.

E Extended Numerical Results: Mixture of Gaussians

We first validate PDI on the problem of sampling from a weighted mixture of Gaussians in \mathbb{R}^d ,

$$f_0(\mathbf{x}) = -\log \sum_{k=1}^K w_k \mathcal{N}(\mathbf{x}; \boldsymbol{\mu}_k, \boldsymbol{\Sigma}_k), \quad (119)$$

truncated to a polytope $\{\mathbf{x} : \mathbf{A}\mathbf{x} \leq \mathbf{b}\}$. The optimization problem is

$$\min_{\mu(\mathbf{x})} \mathbb{E}_{\mathbf{x} \sim \mu} [f_0(\mathbf{x})] \quad \text{s.t.} \quad \mathbb{E}_{\mathbf{x} \sim \mu} [\mathbf{A}^\top \mathbf{x} - \mathbf{b}] \preceq \mathbf{0}, \quad (120)$$

i.e., the sampler must produce a distribution that concentrates on high-density regions of the mixture while satisfying M linear inequality constraints in expectation. This is not an everywhere constrained sampling problem, where each sample $\mathbf{x} \in \mathbb{R}^d$ is required to satisfy the constraints. In (13), the constraints are imposed on average over the target distribution. This allows some samples to violate the constraints while others should be strictly feasible to compensate.

E.1 Baseline configuration

Each baseline shares the evaluation seed, batch size, and diffusion discretisation $T = 500$ where applicable.

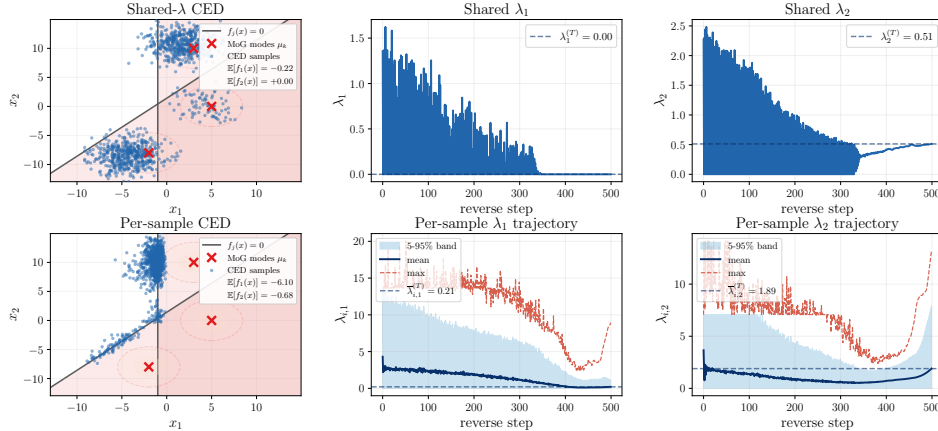


Figure 5: Comparison of **Constrained Energy-based Diffusion-sampler (CED)** in enforcing the constraints in expectation (top) vs per sample (bottom). Per-sample enforcement produces conservative samples that satisfy the constraints individually but fall short in providing a competitive objective.

Unconstrained DM. We run our trained model with $\lambda_t = \mathbf{0}$ for all time steps. This eliminates the constraint term from the energy function, and lets the model sample from the unconstrained Boltzmann density $\exp(-f_0(\mathbf{x})/\beta)$.

PDM. Similarly, we run a reverse process with $\lambda_t = \mathbf{0}, \forall t$. At each step, the Tweedie prediction $\hat{\mathbf{x}}_0$ is projected onto the feasible set before being used in the DDPM posterior,

$$\tilde{\mathbf{x}}_0 = \Pi_{\mathcal{F}}(\hat{\mathbf{x}}_0), \quad \mathcal{F} = \{\mathbf{x} : \mathbf{f}(\mathbf{x}) \preceq \mathbf{0}, j = 1, \dots, M\}. \quad (121)$$

PDM then forces feasibility by construction and is therefore a hard-constraint method, unlike PDI.

PDL. Direct Langevin dynamics in the \mathbf{x} -space with per-sample dual variables:

$$\mathbf{x}_{t+1} = \mathbf{x}_t - \eta_p \nabla_{\mathbf{x}_t} (f_0(\mathbf{x}_t) + \lambda_t^\top \mathbf{f}(\mathbf{x}_t)) + \sqrt{2\eta_p} \epsilon_t, \quad (122)$$

$$\lambda_{t+1} = [\lambda_t + \eta_d \mathbf{f}(\mathbf{x}_{t+1})]_+, \quad (123)$$

where $\epsilon_t \sim \mathcal{N}(0, \mathbf{I})$. The main difference between PDL and PDI is that the former operates in the clean sample space. It therefore uses the gradient of the energy function to update \mathbf{x} . In PDI, the dynamics evolve under a decreasing noise level, and at each time step, we follow the score of the corresponding denoised distribution.

A distinction arises between these baselines and our method PDI. In all the aforementioned updates, the correction is made to each sample individually, forcing all samples to abide by the constraints. Their solutions are therefore feasible in our problem formulation, but suboptimal because they are more conservative. Figure 5 shows a toy example of the problem with $d = 2, K = 3$, and $M = 2$. Per-sample enforcement sacrifices the opportunity to sample from the high-density regions of the MoG while still satisfying the constraints on average. Instead, it concentrates samples near the boundary of the feasible set, shown as the white region.

In the following table, we provide all the hyperparameters of the baselines:

Method	η_d	η_p	T	Diffusion Noise Schedule
PDL	10	10^{-3}	500	—
PDM	—	—	500	cosine
Unconstrained	—	—	500	cosine

E.2 Data and Architecture

The problem consists of a K -component Gaussian mixture, truncated by M halfplane constraints. Mode centers are placed uniformly at random in a ball of radius proportional to a spread parameter,

Table 3: PDI training hyperparameters for the MoG experiment.

Parameter	Value	Parameter	Value
<i>Problem</i>		<i>Training</i>	
Dimension d	30	Optimizer	AdamW
Mixture components K	12	Learning rate	10^{-3}
Constraints M	10	SGD steps	8000 (800×10)
		Batch size B	256
		MC samples K_{MC}	256
		Rollout batch $ \mathcal{B}_{train} $	4 graphs
		Exploitation fraction ρ_{exp}	$0 \rightarrow 0.7$
<i>Diffusion</i>		<i>Training – dual ascent rollouts</i>	
Noise schedule	cosine	Training dual step size η_{train}	0.01
Timesteps T	500	Dual variable cap λ_{max}	50
Inverse temperature β^{-1}	50		
<i>Score network</i>		<i>Training – λ prior</i>	
Architecture	MLP	λ -prior family	$\exp(\nu)$
Hidden dimension	512	ν_{min}	0.1
Number of layers	8	ν_{max}	20.0
Parameters	8.73M		
Conditioning inputs	$(\mathbf{x}_t, t, \lambda)$		
<i>Training – perturbation</i>		<i>Inference</i>	
Perturbation fraction ρ_{pert}	1.0	Inference dual step size η	1.0
\mathbf{x}_t perturbation std ϵ_x	2.0	Initial λ_0	$\mathbf{0}$
λ perturbation std ϵ_λ	5.0	Feasibility tolerance	0.02
		Inverse temperature β^{-1}	50

with isotropic covariances drawn from a specified range. The constraint normals are chosen so that some halfplanes separate pairs of modes while others cut through mode basins, ensuring that constraints are active near high-density regions. Constraint levels \mathbf{b} are calibrated so that a target fraction of modes have infeasible centers and the remaining feasible modes sit close to constraint boundaries. Since this example is used as a proof of concept, the dataset has only one problem instance.

The score network is an MLP with FiLM conditioning. The input (\mathbf{x}_t, λ) is projected into a hidden dimension, added to the sinusoidal timestep embedding, and passed through a stack of residual blocks. Each block applies a linear layer, layer normalization with FiLM modulation from the timestep embedding (scale and shift), and a SiLU activation. The output is projected back to \mathbb{R}^d to predict the noise ϵ_t .

E.3 Hyperparameter Choices

We ran a sweep over the hyperparameters: $\beta, T, \eta, \rho, K_{MC}, \nu_{max}, \epsilon_x,$ and ϵ_λ , and Table 3 shows the values we use in our experiments. All experiments were run on a single NVIDIA GeForce RTX 3090 card.

E.4 Additional Results

We also record the input-to-output transition matrix and report it in Figure 6. The figure shows that PDL divides the mass between one mode (#10) and the diagonal of the transition matrix. The mass on the diagonal indicates that each input sample typically converges to its nearest mode. In contrast, PDI does not exhibit this behavior. This is partly due to the noise injected along the reverse trajectory, which acts as an annealing mechanism and allows samples to move across modes. It is also due to the entropy regularization in the PDI formulation, controlled by the temperature parameter, which encourages a distributional solution rather than deterministic convergence to the nearest mode. This temperature-driven randomization is absent in PDL.

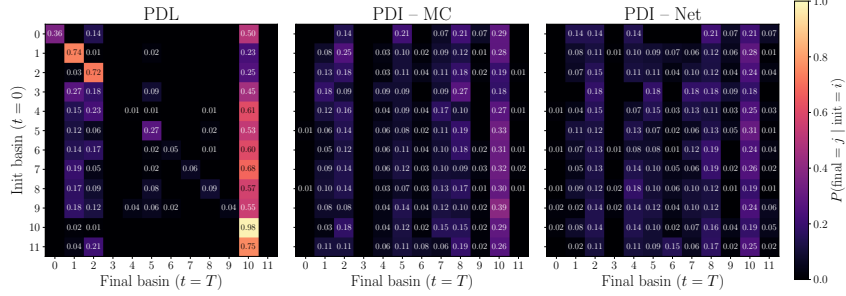


Figure 6: **Initial to final transition matrix.** The matrix is almost diagonal in the PD Langevin case, reflecting the fact that samples converge to their nearest modes.

F Extended Numerical Results: Wireless Resource Allocation

We study stochastic constrained optimization for optimal wireless resource allocation [7, 30, 60].

Consider an ad-hoc wireless network comprised of $N = 200$ transmitter-receiver (tx-rx) pairs deployed uniformly over a square area of side length $R = 5800$ meters, yielding an average density of $\nu = 5.9$ tx-rx pairs/km². Each transmitter communicates with a single designated receiver, and each receiver treats incoming signals from all other transmitters as interference. The resource allocation (optimization) variable is the transmit power vector $\mathbf{x} \in [0, P_{\max}]^N$, where $P_{\max} = 10$ mW.

Channel model. The channel model includes both large-scale and small-scale fading effects. We denote by h_{ij} the large-scale channel gain from transmitter i to receiver j , governed by a dual-slope path-loss model with log-normal shadowing of standard deviation $\sigma = 7$ dB. A *network configuration* $\mathbf{H} \in \mathbb{R}_+^{N \times N}$ is the matrix of all large-scale gains $[\mathbf{H}]_{ij} = h_{ij}$, and it is jointly determined by the random geometric deployment of the tx-rx pairs, which fixes the pairwise distances and hence the path-loss components, and the realization of the log-normal shadowing. Each network configuration \mathbf{H} remains fixed over the operating horizon, while the small-scale fading, which follows a Rayleigh distribution with a pedestrian velocity of 1 m/s, produces time-varying instantaneous channel gains $h_{ij,t}$ at each time slot t of duration 50 milliseconds. We set the channel bandwidth to $W = 40$ MHz and the noise power spectral density to $N_0 = -174$ dBm/Hz.

Given an allocation \mathbf{x}_t and fading realization \mathbf{H}_t at time slot t , the instantaneous rate of receiver j is

$$\tilde{r}_j(\mathbf{x}_t, \mathbf{H}_t) = \log_2 \left(1 + \frac{[\mathbf{x}_t]_j \cdot |h_{jj,t}|^2}{WN_0 + \sum_{i \neq j} [\mathbf{x}_t]_i \cdot |h_{ij,t}|^2} \right). \quad (124)$$

The ergodic rate of receiver j is obtained by averaging the instantaneous rates over T time slots, i.e., $r_j \approx (1/T) \sum_{t=1}^T \tilde{r}_j(\mathbf{x}_t, \mathbf{H}_t)$.

Optimization objective. For a given network state \mathbf{H} , the goal is to maximize the ergodic sum-rate subject to per-user minimum ergodic rate constraints. That is,

$$P_{\text{pc}}^* = \max_{\mu(\mathbf{x})} \mathbf{1}^\top \mathbf{r}(\mu, \mathbf{H}) + \beta \mathcal{H}(\mu), \quad \text{s.t.} \quad \mathbf{r}(\mu, \mathbf{H}) \geq \mathbf{1} \cdot r_{\min}, \quad (125)$$

where μ denotes a power allocation policy, and r_{\min} is the minimum ergodic rate requirement. The solution to this problem is rarely a degenerate policy. Because users compete for the same communication resources and interfere with one another, it is generally impossible for all users to transmit at high power simultaneously while satisfying their rate requirements. The optimal policy is therefore often a switching policy, where different users are activated at different times so that each receives enough transmission opportunities to meet its rate constraint on average. This naturally leads to a multimodal optimal distribution, with different modes corresponding to different active-user patterns.

F.1 Data and Architecture

Dataset Generation. We generate a dataset of 256 network configurations in total, viewed as independent samples from the underlying distribution of network configurations induced by the random geometry of tx-rx deployments and random shadowing for the given value of R . A 5:1:2 train-validation-test split results in a training dataset of $|\mathcal{D}| = 160$ networks, $|\mathcal{V}_{\text{val}}| = 32$ validation networks, and $|\mathcal{T}| = 64$ test networks.

Graph representation. We represent each network configuration \mathbf{H} as a directed graph $\mathcal{G}_{\mathbf{H}} = (\mathcal{V}, \mathcal{E}, \mathbf{w})$, where the node set $\mathcal{V} = \{1, \dots, N\}$ corresponds to the tx-rx pairs. We assign each directed edge $(i, j) \in \mathcal{E}$ a weight proportional to the log-normalized channel gain given by

$$e_{ij} \propto \log_2 \left(1 + \frac{P_{\max} |h_{ij}|^2}{WN_0} \right), \quad (126)$$

and sparsify the graph by thresholding the weak edges so that we retain only the top-10 strongest incoming edges per receiver node.

Graph Neural Networks (GNNs). The power allocations \mathbf{x} and ergodic rate vectors \mathbf{r} are naturally interpreted as node-level signals supported on $\mathcal{G}_{\mathbf{H}}$. We therefore use GNNs as the base parameterization for the score model, which takes the problem representation $\mathcal{G}_{\mathbf{H}}$ as input. We implement graph convolutions using Torch Geometric’s TAGConv (with $K=2$). The model consists of $L=8$ TAGConv residual blocks with hidden dimension $d_h=256$.

The timestep information is injected through Feature-wise Linear Modulation (FiLM). The dual variable $\boldsymbol{\lambda} \in \mathbb{R}^N$ is concatenated to the input features \mathbf{x} .

F.2 Baselines

PDM. We run our trained score model with $\boldsymbol{\lambda}_t = \mathbf{0}$ for all the denoising steps to eliminate the dual ascent. After each step, we perform a projection into the feasible set by solving the augmented-Lagrangian problem:

$$\mathbf{x}_t \leftarrow \arg \min_{\mathbf{w}} \|\mathbf{w} - \mathbf{x}_t\|^2 + \frac{\zeta}{2} \|[\mathbf{f}(\mathbf{w})]_+\|^2, \quad (127)$$

where $[\mathbf{x}]_+ = \max\{\mathbf{0}, \mathbf{x}\}$. We solve the problem via a few steps of gradient descent.

DPS. We run a reverse process with our trained score model while forcing $\boldsymbol{\lambda}_t = \mathbf{0}, \forall t$, to eliminate the dual ascent. At each step in the inference process, the prediction \mathbf{x}_t is corrected by a gradient step that penalizes constraint violation before it is fed to the next iteration,

$$\mathbf{x}_t \leftarrow \mathbf{x}_t - s_t \nabla_{\mathbf{x}_t} \|\mathbf{f}(\mathbf{x}_t)\|^2. \quad (128)$$

The gradient is applied directly to the denoised signal at the end of each step, and weighted by a scalar step size s_t . The step size is set to the inverse of the noise variance at each denoising step.

ST & PD Expert Policy. Following the methodology in [30], for each training network $\{\mathbf{H}^{(b)}\}_{b \in \mathcal{D}}$, we solve the power control problem using an expert algorithm, specifically a dual gradient descent algorithm. The expert algorithm generates trajectories of primal iterates that are near-optimal and feasible in the ergodic sense. We view these iterates as draws from a stochastic, optimal policy, collecting $M = 200$ samples from the convergence regime of the algorithm to obtain an expert dataset of resource allocation vectors $\{\mathbf{x}^{(m)}(\mathbf{H}^{(b)})\}_{m=1}^M$.

We train a diffusion model to imitate the expert data generated by the PD Expert. The neural network $\epsilon_{\theta}(\mathbf{x}_t, t)$ is trained via the standard denoising score matching objective and sampled using the deterministic DDIM update:

$$\mathbf{x}_{t-1} = \sqrt{\bar{\alpha}_{t-1}} \hat{\mathbf{x}}_0 + \sqrt{1 - \bar{\alpha}_{t-1}} \epsilon_{\theta}(\mathbf{x}_t, t). \quad (129)$$

This method has no explicit constraint enforcement mechanism; feasibility depends entirely on the training data distribution and the expressivity of the parameterization.

In order to replicate the performance of [30], we use the U-Graph Neural Network (U-GNN) parametrization proposed therein, which was designed for graph signal diffusion. This ensures that

Table 4: Baseline hyperparameters for the wireless allocation experiment. The DT settings differ from PDI in Table 6; all other problem, diffusion, architecture, and evaluation settings are identical.

Parameter	Value	Parameter	Value
<i>ST</i>		<i>PDL</i>	
Backbone	UGNN [30]	Iterations	500
Base channels / levels	64 / 4	Primal learning rate η_p	10^{-4}
Graph filter	$K = 2$ hops	Dual learning rate η_d	1
Layers per level	2	Initial value λ_0	0
Timesteps T	500		
Noise schedule	Linear		
Optimizer	AdamW ($\beta_1 = 0.9, \beta_2 = 0.98$)		
Learning rate / weight decay	$10^{-4} / 10^{-4}$		
LR schedule	Cosine		
Batch size	960		
Conditioning	3 channels ($\mathbf{x}, t, \mathcal{G}$)		
Epochs	5000		
<i>PDM</i>		<i>DPS</i>	
Base model	PDI-Net with $\lambda = 0$	Base model	PDI-Net with $\lambda = 0$
Projection iterations	100		
Projection step size	0.05		
Regularization ζ	30		
<i>DT</i>			
Score model	Same PDI-Net architecture	Outer iterations D	4000
Conditioning channels	3 ($\mathbf{x}, t, \mathcal{G}$)	Inner SGD steps E	10
Dual input	none	Minibatch size $ \mathcal{B}_{\text{train}} $	4 problems
Samples per network I	20	Initial λ_0	10
λ update batch size $ \mathcal{B}_\lambda $	16 problems	Dual learning rate η_{DT}	0.1

the DDIM imitation baseline follows the original architectural setup. We do not use U-GNN as the base parametrization for our method because it is computationally heavy. Instead, we use a vanilla GNN, since PDI enforces the constraints through dual ascent during sampling and therefore does not need to rely solely on a highly expressive score parametrization for feasibility.

DT. The training procedure is described in Appendix D. The score model shares the same architecture as PDI-Net, except that it uses three conditioning channels instead of four.

All hyperparameters of these baselines are given in Table 4.

F.3 Additional Results

Dual training (continued). We investigate the difference between PDI and DT more closely by comparing the dual trajectories. Figure 7 plots the cosine similarity and the L_2 distance between the dual variables generated along the DT trajectory and the last dual iterate obtained by the PDI dynamics. These quantities are averaged over the training examples. We use the training dataset because DT does not infer dual variables during inference.

The cosine similarity reaches its maximum between the epochs 2200 and 3200, after which the DT dual variables begin to drift away from the PDI dual variables. We therefore save all DT checkpoints after epoch 2200, evaluate them on the test set and report the resulting metrics in Figure 8. The figure shows that all DT checkpoints achieve higher mean rates (objective) than PDI, shown by the dashed blue line. This suggests that the models offer higher mean rates by

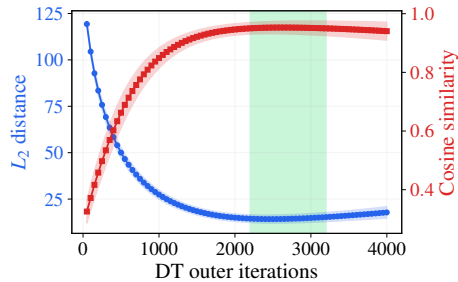


Figure 7: **Dual Training.** Cosine similarity and L_2 distance between the dual variables across the DT training iterations and the last-iterate PDI dual variables. The shaded region indicates the training iterations where the cosine similarity peaks above 0.95. The metrics then drift slightly afterwards.

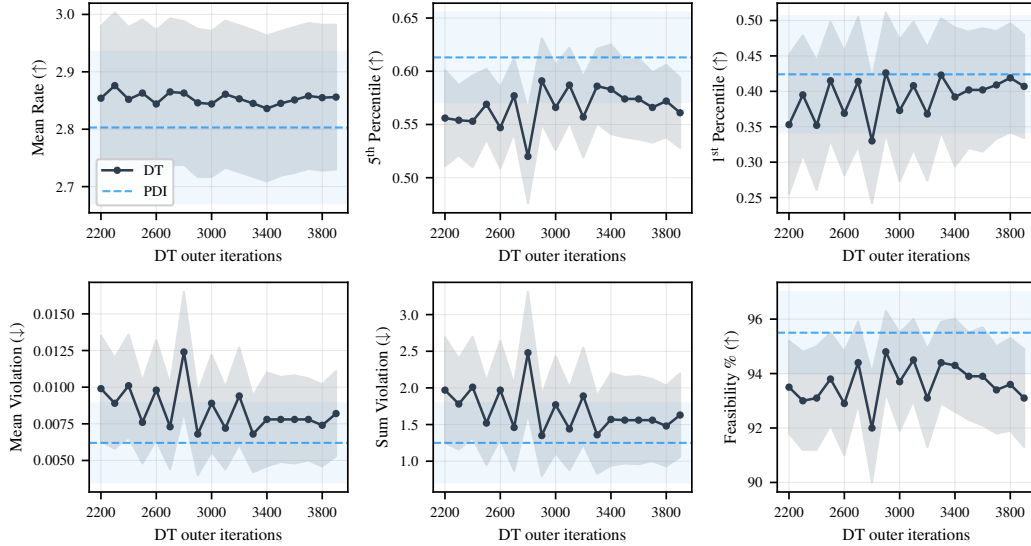


Figure 8: **Performance of DT checkpoints along the training trajectory.** The DT models fail to attain the same 5th percentile rates, mean violations and feasibility percentage as PDI. All the metrics are evaluated over the test set.

Table 5: **DT after extra training at fixed dual variables (DT+).** We continue training several DT checkpoints with no dual updates and report the best two results (corresponding to iterations 2200 and 2900). PDI achieves comparable performance with much lighter training.

Method	Mean rates (↑)	5th%ile rate (↑)	1st%ile rate (↑)	Mean viol. (↓)	Sum viol. (↓)
PDI-Net	2.803 ± 0.132	0.613 ± 0.042	0.424 ± 0.082	0.0062 ± 0.0027	1.25 ± 0.54
DT+ (2200)	2.814 ± 0.128	0.656 ± 0.051	0.426 ± 0.112	0.0060 ± 0.0029	1.19 ± 0.59
DT+ (2900)	2.822 ± 0.128	0.615 ± 0.045	0.422 ± 0.090	0.0063 ± 0.0028	1.25 ± 0.57

reducing interference through more conservative power allocations. This reduction in interference benefits some users but sacrifices tail performance. This is reflected in the lower fifth and first percentile rates and feasibility percentages across all checkpoints.

These observations suggest that the dual variables generated by DT do not induce the same primal solutions obtained by PDI dynamics. This can be attributed to the fact that the PDI score field is conditioned on the current dual variable λ_t while that of DT is an unconditional score field obtained after training over a history of changing dual variables. Therefore, even when the DT dual variable is close to the PDI dual variable, the checkpoint at that epoch does not need to approximate the score field associated with that particular dual variable. The reason is that the checkpoint represents the accumulated effect of the preceding training trajectory, not a score model explicitly indexed by the current dual variable.

To further separate the quality of the learned dual variables from the quality of the corresponding score model, we continue training several DT checkpoints for extra 1000 outer iterations while freezing their dual variables. We refer to the resulting models as DT+. This experiment asks whether the dual variables produced by DT are useful once the score model is given enough optimization time to adapt to them. Table 5 reports the two best DT+ models and shows a substantial improvement over the original DT checkpoints. This indicates that DT can reach informative dual variables, but the score model at the corresponding checkpoint has not necessarily learned the score field induced by that dual value. Rather, because the model is updated only partially while the dual variables evolve, the checkpoint reflects the accumulated effect of the preceding training trajectory. In this sense, practical DT behaves as a score model shaped by a history of dual variables, and not as a fully optimized score model for the current dual variable. The improvement of DT+ also comes with a much larger training cost (4000 original outer iterations in addition to extra 1000 iterations for tuning the model), whereas PDI reaches comparable performance using only 400 training outer iterations.

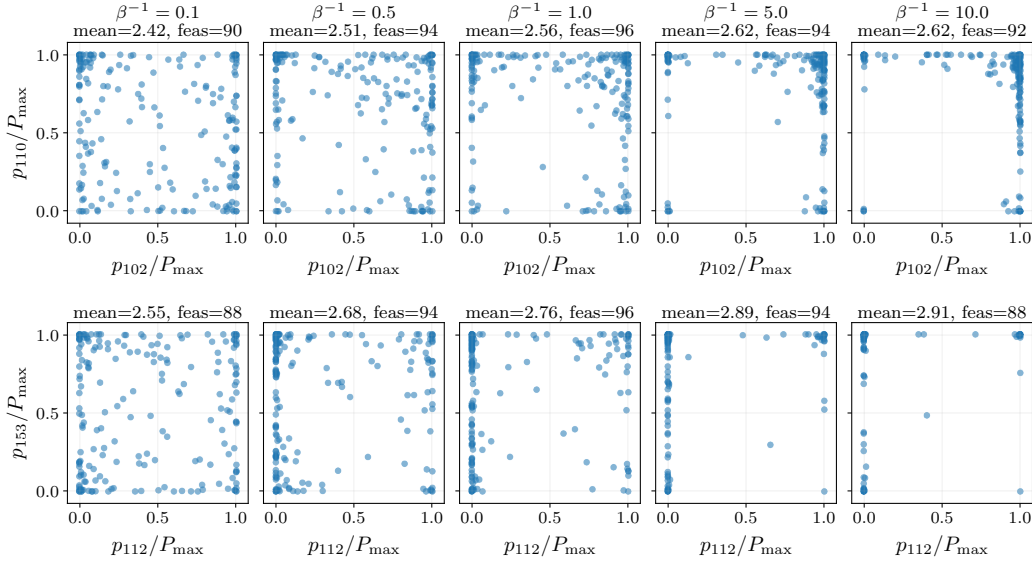


Figure 9: **Temperature effect.** Two-dimensional scatter plots of generated samples of two test networks. The title shows the mean rates and feasibility of the network. Higher temperature (left) promotes more diverse allocations while lower temperature (right) generates more degenerate samples. The value $\beta = 1$ provides a good balance between mean rates and feasibility.

The improvement of DT+ shows that the dual variables produced by DT are informative. However, it does not remove the limitation of using an unconditional score model. Since DT does not take the dual variable as input, the correction induced by the dual trajectory is absorbed into the score-model parameters rather than represented explicitly. This can work well for problem instances whose required correction is close to the one encoded by the trained model. At inference, however, new problem instances may induce different optimal multipliers or different constraint residuals along the denoising trajectory. The DT score field cannot adapt to these instance-dependent corrections during sampling, because the dual variable is not provided to the model.

PDI reduces this limitation by learning a λ -conditioned family of score fields. During inference, the current dual iterate is passed directly to the score model, so each reverse step uses a score field matched to the dual correction used at that step. This does not mean that PDI samples from the Gibbs distribution of one fixed dual variable, since the final sample is produced by a sequence of kernels conditioned on different dual iterates. Rather, the advantage is that the constraint correction and denoising dynamics remain coupled along the trajectory, allowing constraint violations to influence subsequent denoising steps more directly.

Temperature effect. In Figure 9, we analyze the effect of the temperature parameter β . Large β , equivalently small β^{-1} , generate more uniform samples, which cause severe interference and in turn the lowest mean rates and feasibility. Lower temperatures produce more degenerate distributions that concentrate the samples at the corners. This prevents severe interference and provides better mean rate, but does not fully benefit from time sharing (i.e., low feasibility). We find that $\beta = 1$ in this experiment balances the mean rates with feasibility.

Noise annealing effect. PDI differs from PDL because it follows the score fields of a sequence of progressively denoised distributions, rather than the score field of the clean target distribution. This mechanism is reminiscent of simulated annealing. Early noisy diffusion steps smooth the target landscape and promote exploration across modes, while later low-noise steps gradually sharpen the distribution and refine the samples toward the constrained target. Unlike classical simulated annealing, however, the annealing in PDI is induced by the diffusion noise schedule rather than by the temperature of the energy function. Figure 10 shows this effect, represented in the diverse samples generated by PDI compared with the more concentrated samples produced by PDL.

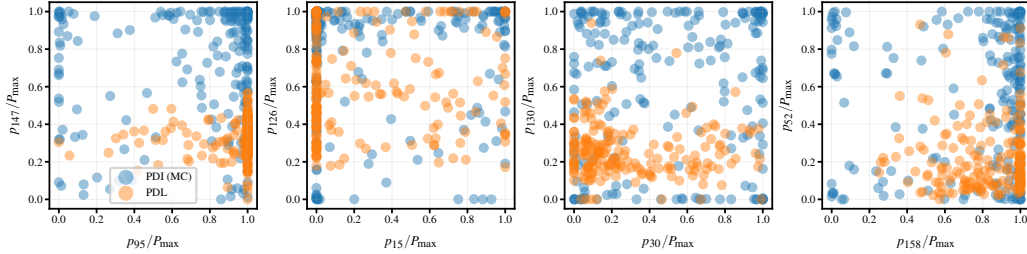


Figure 10: **Annealing effect of PDI.** A scatter plot of the predicted power allocation of four pairs of agents. PDI discovers more transmission modes, allowing more agents to transmit with higher power to achieve higher rates on average. PDL concentrates the samples in the same modes.

Table 6: PDI hyperparameters for the wireless power allocation experiment.

Parameter	Value	Parameter	Value
<i>Problem setup</i>		<i>Training</i>	
Number of users N	200	Optimizer	AdamW
Max transmit power P_{\max}	10 dBm	Learning rate	10^{-3} ($\rightarrow 10^{-5}$)
Bandwidth	40 MHz	Weight decay	10^{-4}
Minimum rate r_{\min}	0.6 bps/Hz	Outer iterations N_{outer}	400
Number of networks	256		
<i>Score network</i>		<i>Training</i>	
Hidden dimension	256	Inner SGD steps N_{inner}	10 \rightarrow 30
GNN layers	8	Batch size $ \mathcal{B}_{\text{train}} $	4 problems
Filter order K	2	Replay buffer capacity $ \mathcal{B} $	4 096
Time embedding dimension	128	Minibatch size B	128
Conditioning channels	4 ($\mathbf{x}, t, \lambda, \mathcal{G}$)		
Activation / normalization	SiLU / LayerNorm		
<i>Diffusion process</i>		<i>Training – perturbation and prior</i>	
Timesteps T	500	Exploitation fraction ρ_{exp}	0 \rightarrow 0.7
Noise schedule	Cosine	λ prior range $[\nu_{\min}, \nu_{\max}]$	[2, 10]
MC candidates K_{MC}	8	Perturbation std ($\epsilon_{\mathbf{x}}/\epsilon_{\lambda}$)	0.1/0.5
		Perturbation fraction ρ_{pert}	0.5
<i>Dual variable (inference)</i>		<i>Evaluation</i>	
Inverse temperature β^{-1}	1.0	Policies per network K	200
Step size η_t	0.05	Time-sharing timeslots R_{eval}	500
Initialization λ_0	10.0	Test networks	64
Clamp λ_{\max}	50	Evolution trials	50
Sub-batch groups C	10		

F.4 Hyperparameters Choices

Table 6 collects the hyperparameters of the problem and PDI training. All experiments were run on a single NVIDIA GeForce RTX 3090 card.

G Extended Numerical Results: Portfolio Management

In constrained portfolio optimization, we aim to allocate weights $\mathbf{x} \in \Delta^{N-1}$ across $N = 500$ assets, organized in 10 sectors. The return \mathbf{r} is drawn from a factor model with mean μ and block-diagonal covariance Σ . Our objective is to maximize expected return subject to per-asset variance-risk budgets, i.e.,

$$P_{\text{pm}}^* = \max_{\mu(\mathbf{x})} \mathbb{E}_{\mathbf{x} \sim \mu} [\mathbb{E}_{\mathbf{r}}[\mathbf{r}^T \mathbf{x}]] + \beta \mathcal{H}(\mu) \quad \text{s.t.} \quad \mathbb{E}_{\mathbf{x} \sim \mu} [x_j (\Sigma \mathbf{x})_j] \leq b_j, \quad j = [N], \quad (130)$$

The budget $b_j > 0$ caps how much variance asset j is permitted to contribute in expectation over all portfolios. In practice, portfolio construction is rarely a single-solution problem. Even under common market assumptions, different clients or rebalancing instances may require different allocations due to

Table 7: Baseline hyperparameters in the portfolio management problem.

Parameter	Value	Parameter	Value
<i>PD-Langevin</i>			
Primal step size η_p	10^{-2}	Iterations	500
Dual step size η_d	100		
<i>PDM</i>			
Projection iterations	50	λ (net input)	0
<i>PDI-MC</i>			
Inverse temperature β^{-1}	2 000	dual step size η_t	300
MC candidates K_{MC}	512	λ_{decay}	0.001
<i>Evaluation</i>			
Generated samples	1024	Test instances	20

heterogeneous preferences, liquidity needs, tax considerations, and model uncertainty. This motivates learning a distribution over portfolios rather than a single deterministic allocation. The average risk constraints allow the sampler to trade risk across different portfolio samples, admitting occasional high-risk, high-return allocations while ensuring that the overall exposure of each asset remains within its prescribed budget in expectation.

G.1 Data & Architecture

Data. We generate synthetic portfolio instances using a latent factor model with sector structure. Each instance consists of $N = 500$ assets organized into $S = 10$ sectors. Each asset’s log-returns are drawn from a multivariate normal with a sector-structured covariance matrix Σ , where assets within the same sector are more correlated with each other than with assets in other sectors. We draw 1000 return scenarios and convert to simple returns via exponentiation.

Graph construction. To construct the graph, we compute the absolute correlation matrix from Σ , remove self-loops, and for each asset retain edges to its k -nearest neighbors (we use $k=20$) by absolute correlation magnitude. Edge weights are normalized by the largest eigenvalue of the resulting adjacency matrix.

Conditioning and architecture. We use the same GNN architecture used in the wireless allocation problem. The timestep information is injected through Feature-wise Linear Modulation (FiLM). The shared dual variable $\lambda \in \mathbb{R}^N$ is concatenated to the input features. The network comprises $L=6$ residual blocks with hidden dimension $d_h=128$.

G.2 Baselines

The hyperparameters of the baselines are summarized in Table 7.

G.3 Additional Results

We ran additional experiments to evaluate different aspects of our algorithm, and the results match our previous findings.

First, we compare the full PDI algorithm with variants that freeze the dual variable after an initial primal-dual run and report the results in Figure 11. In this experiment, we consider the last dual iterate and the time-averaged dual variable. The results show that the time-averaged multiplier performs better than the last iterate. This is consistent with our convergence result, which guarantees convergence for the time-average of the dual variables rather than for the final iterate itself. However, both fixed-dual variants remain below the full PDI performance. We also notice that the initial λ_0 does not affect the PDI trajectory. This suggests that PDI is not simply estimating one good multiplier and then sampling from it. Its advantage comes from updating the multiplier throughout the denoising trajectory.

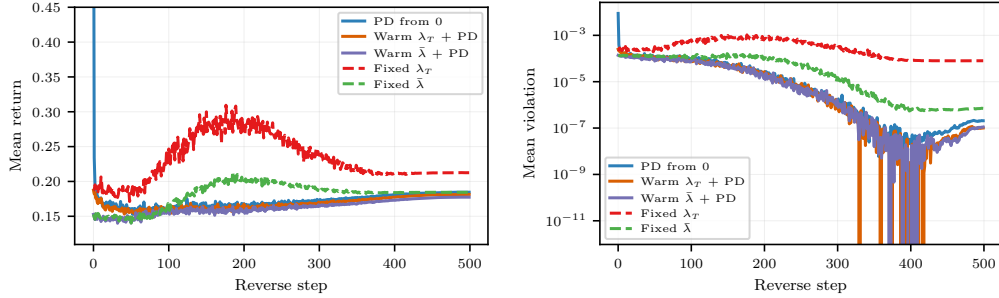


Figure 11: **Performance of PDI while fixing λ along the diffusion steps.** The time-average dual variable gives better objective and constraint satisfaction compared to the last iterate. However, running the dual updates beats both of them and does not depend on the initial value.

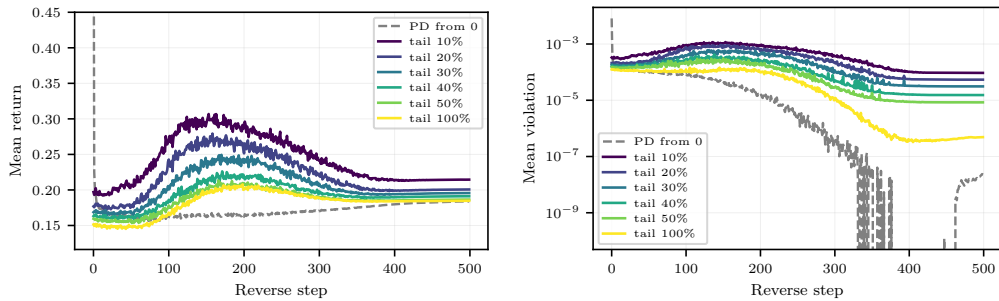


Figure 12: **Frozen $\bar{\lambda}_{\text{tail}}$ during sampling.** The effect of running the sampler with a fixed dual variable equal to the time-average of the tail dual iterates.

Second, we test in Figure 12 whether using only a late-stage average of the dual trajectory is enough. The answer is negative. The performance degrades when the average is computed only over a suffix of the trajectory. This suggests that the early dual iterates are not merely transient noise; they contribute to the effective multiplier that governs the sampled distribution. In other words, the full trajectory matters, but its aggregate effect can be captured well by the full time-average.

Our third experiment in Figure 13 investigates the role of the entropy regularization on the final solutions and trajectories. The figure shows that when the temperature β is high, the sampler produces more diverse samples, but the objective can be weaker. When the temperature is lower, the distribution becomes more concentrated around high-quality solutions. This improves the objective, but it can also make the dynamics sharper and more sensitive.

Finally, the noise-schedule comparisons of Figure 14 show that the schedule is important for convergence. Schedules that keep the process noisy for longer, such as the standard cosine and DDPM linear schedules, give more stable behavior and better feasibility. In contrast, schedules that reconstruct the clean sample too early make the sampler sensitive before the dual variable has stabilized. This leads to larger violations and weaker convergence. These results agree with Theorem 2, which suggests that early high-noise steps damp the effect of dual mismatch, while later low-noise steps should only occur after the dual variable has moved close to a good region.

G.4 Hyperparameter Choices

We ran a sweep over β and η_t . Table 8 displays all hyperparameters used in experiments. All experiments were run on a single NVIDIA GeForce RTX 3090 card.

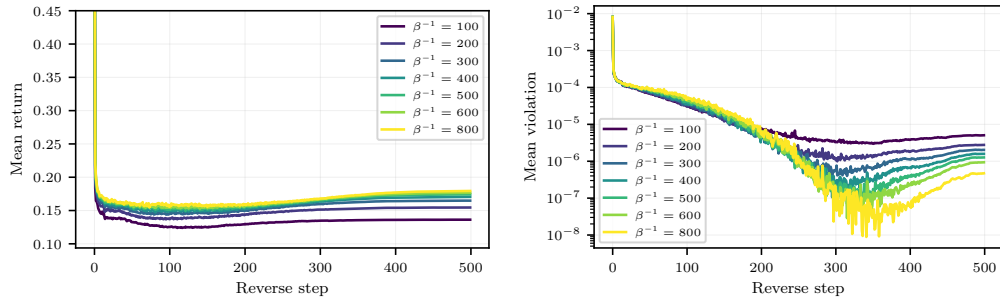


Figure 13: **Temperature effect.** Lower temperature β , equivalently larger β^{-1} (yellow) helps improve returns and constraint satisfaction.

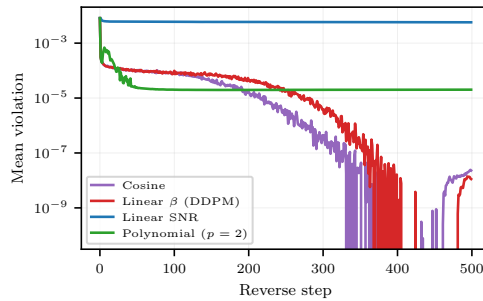


Figure 14: **Effect of noise schedules.** Standard DDPM cosine and linear schedules give better feasibility. Schedules that reconstruct the clean sample too early make the sampler sensitive to perturbations in the dual variable before the dual variable has stabilized.

Table 8: PDI hyperparameters in the portfolio management problem (training and inference).

Parameter	Value	Parameter	Value
<i>Diffusion process</i>		<i>Training</i>	
Timesteps T	500	Optimizer	AdamW
Noise schedule	Cosine	Learning rate	$3 \times 10^{-4} \rightarrow 3 \times 10^{-5}$ (cosine)
Inverse temperature β^{-1}	2 000	λ prior $[\nu_{\min}, \nu_{\max}]$	[150, 1500]
MC candidates K_{MC}	512	λ perturbation (mult.) ϵ_λ	0.3
		Exploitation ratio ρ_{exp}	$0 \rightarrow 0.7$
		Minibatch size B	128
		Training instances	200
<i>Dual variable (inference)</i>		<i>Training</i>	
Step size η_t	300	Validation instances	10
Initialization λ_0	0	Inner SGD steps N_{inner}	$10 \rightarrow 100$
Clamp λ_{max}	10^4	Outer iterations N_{outer}	600
Weight decay	0.001	Replay buffer capacity	8 192
		Rollout minibatch $ \mathcal{B}_{\text{train}} $	4 problems
<i>Score network</i>			
Backbone	GNN		
Hidden dimension d_h	128		
Residual blocks L	6		
Graph filter order K	2		
Graph sparsity (top- k)	20		
Conditioning	FiLM + λ concat		